Rolling Bearing Analysis

Fifth Edition

Tedric A. Harris
Michael N. Kotzalas

CRC Press
Taylor & Francis Group

Rolling Bearing Analysis

FIFTH EDITION

Advanced Concepts of Bearing Technology

Tedric A. Harris
Michael N. Kotzalas

CRC Taylor & Francis
Taylor & Francis Group

Rolling Bearing Analysis

FIFTH EDITION

Advanced Concepts of Bearing Technology

Rolling Bearing Analysis

FIFTH EDITION

Advanced Concepts of Bearing Technology

Tedric A. Harris
Michael N. Kotzalas

Taylor & Francis
Taylor & Francis Group
Boca Raton London New York

CRC is an imprint of the Taylor & Francis Group, an informa business

CRC Press
Taylor & Francis Group
6000 Broken Sound Parkway NW, Suite 300
Boca Raton, FL 33487-2742

Printed in the United States of America on acid-free paper
10 9 8 7 6 5 4 3 2 1

International Standard Book Number-10: 0-8493-7182-1 (Hardcover)
International Standard Book Number-13: 978-0-8493-7182-0 (Hardcover)

Preface

The main purpose of the first volume of this handbook was to provide the reader with information on the use, design, and performance of ball and roller bearings in common and relatively noncomplex applications. Such applications generally involve slow-to-moderate speed, shaft, or bearing outer ring rotation; simple, statically applied, radial or thrust loading; bearing mounting that does not include misalignment of shaft and bearing outer-ring axes; and adequate lubrication. These applications are generally covered by the engineering information provided in the catalogs supplied by the bearing manufacturers. While catalog information is sufficient to enable the use of the manufacturer's product, it is always empirical in nature and rarely provides information on the geometrical and physical justifications of the engineering formulas cited. The first volume not only includes the underlying mathematical derivations of many of the catalog-contained formulas, but also provides means for the engineering comparison of rolling bearings of various types and from different manufacturers.

Many modern bearing applications, however, involve machinery operating at high speeds; very heavy combined radial, axial, and moment loadings; high or low temperatures; and otherwise extreme environments. While rolling bearings are capable of operating in such environments, to assure adequate endurance, it is necessary to conduct more sophisticated engineering analyses of their performance than can be achieved using the methods and formulas provided in the first volume of this handbook. This is the purpose of the present volume.

When compared with its earlier editions, this edition presents updated and more accurate information to estimate rolling contact friction shear stresses and their effects on bearing functional performance and endurance. Also, means are included to calculate the effects on fatigue endurance of all stresses associated with the bearing rolling and sliding contacts. These comprise stresses due to applied loading, bearing mounting, ring speeds, material processing, and particulate contamination.

The breadth of the material covered in this text, for credibility, can hardly be covered by the expertise of the two authors. Therefore, in the preparation of this text, information provided by various experts in the field of ball and roller bearing technology was utilized. Contributions from the following persons are hereby gratefully acknowledged:

Neal DesRuisseaux	bearing vibration and noise
John I. McCool	bearing statistical analysis
Frank R. Morrison	bearing testing
Joseph M. Perez	lubricants
John R. Rumierz	lubricants and materials
Donald R. Wensing	bearing materials

Finally, since its initial publication in 1967, *Rolling Bearing Analysis* has evolved into this 5th edition. We have endeavored to maintain the material presented in an up-to-date and useful format. We hope that the readers will find this edition as useful as its earlier editions.

Tedric A. Harris
Michael N. Kotzalas

Authors

Tedric A. Harris is a graduate in mechanical engineering from the Pennsylvania State University, who received a B.S. in 1953 and an M.S. in 1954. After graduation, he was employed as a development test engineer at the Hamilton Standard Division, United Aircraft Corporation, Windsor Locks, Connecticut, and later as an analytical design engineer at the Bettis Atomic Power Laboratory, Westinghouse Electric Corporation, Pittsburgh, Pennsylvania. In 1960, he joined SKF Industries, Inc. in Philadelphia, Pennsylvania as a staff engineer. At SKF, Harris held several key management positions: manager, analytical services; director, corporate data systems; general manager, specialty bearings division; vice president, product technology & quality; president, SKF Tribonetics; vice president, engineering & research, MRC Bearings (all in the United States); director for group information systems at SKF headquarters, Gothenburg, Sweden; and managing director of the engineering & research center in the Netherlands. He retired from SKF in 1991 and was appointed as a professor of mechanical engineering at the Pennsylvania State University at University Park. He taught courses in machine design and tribology and conducted research in the field of rolling contact tribology at the university until retirement in 2001. Currently, he is a practicing consulting engineer and, as adjunct professor in mechanical engineering, teaches courses in bearing technology to graduate engineers in the university's continuing education program.

Harris is the author of 67 technical publications, mostly on rolling bearings. Among these is the book *Rolling Bearing Analysis*, currently in its 5th edition. In 1965 and 1968, he received outstanding technical paper awards from the Society of Tribologists and Lubrication Engineers and in 2001 from the American Society of Mechanical Engineers (ASME) Tribology Division. In 2002, he received the outstanding research award from the ASME.

Harris has served actively in numerous technical organizations, including the Anti-Friction Bearing Manufacturers' Association, ASME Tribology Division, and ASME Research Committee on Lubrication. He was elected ASME Fellow Member in 1973. He has served as chair of the ASME Tribology Division and as chair of the Tribology Division's Nominations and Oversight Committee. He holds three U.S. patents.

Michael N. Kotzalas graduated from the Pennsylvania State University with a B.S. in 1994, M.S. in 1997, and Ph.D. in 1999, all in mechanical engineering. During this time, the focus of his study and research was on the analysis of rolling bearing technology, including quasidynamic modeling of ball and cylindrical roller bearings for high-acceleration applications and spall progression testing and modeling for use in condition-based maintenance algorithms.

Since graduation, Dr. Kotzalas has been employed by The Timken Company in research and development and most recently in the industrial bearing business. His current responsibilities include advanced product design and application support for industrial bearing customers, while the previous job profile in research and development included new product and analysis algorithm development. From these studies, Dr. Kotzalas has received two U.S. patents for cylindrical roller bearing designs.

Outside of work, Dr. Kotzalas is also an active member of many industrial societies. As a member of the ASME, he currently serves as the chair of the publications committee and as a member of the rolling element bearing technical committee. He is a member of the awards committee in the Society of Tribologists and Lubrication Engineers (STLE). Dr. Kotzalas has

also published ten articles in peer-reviewed journals and one conference proceeding. Some of his publications were honored with the ASME Tribology Division's Best Paper Award in 2001 and STLE's Hodson Award in 2003 and 2006. Also, working with the American Bearing Manufacturer's Association (ABMA), Dr. Kotzalas is one of the many instructors for the short course ''Advanced Concepts of Bearing Technology''.

Table of Contents

1 Distribution of Internal Loading in Statically Loaded Bearings: Combined Radial, Axial, and Moment Loadings—Flexible Support of Bearing Rings

LIST OF SYMBOLS

Symbol	Description	Units
A	Distance between raceway groove curvature centers	mm (in.)
B	$f_i + f_o - 1$	
c	Crown drop at end of roller or raceway effective length or crown gap at other locations	mm (in.)
C	Influence coefficient	mm/N (in./lb)
D	Ball or roller diameter	mm (in.)
D_{ij}	Influence coefficient to calculate nonideal roller–raceway contact deformations	
d_m	Bearing pitch diameter	mm (in.)
e	Eccentricity of loading	mm (in.)
E	Modulus of elasticity	MPa (psi)
f	r/D	
F	Applied load	N (lb)
F_a	Friction force due to roller end–ring flange sliding motions	N (lb)
h	Roller thrust couple moment arm	mm (in.)
I	Ring section moment of inertia	mm^4 ($in.^4$)
k	Number of laminae	
K	Load–deflection factor, axial load–deflection factor	N/mm^n ($lb/in.^n$)
l	Roller length	mm (in.)
M	Moment	N × mm (lb × in.)
n	Load–deflection exponent	
P_d	Diametral clearance	mm (in.)
q	Load per unit length	N/mm (lb/in.)
Q	Ball or roller–raceway normal load	N (lb)
Q_a	Roller end–ring flange load in cylindrical roller bearing	N (lb)
Q_f	Roller end–ring flange load in tapered roller bearing	N (lb)

r	Raceway groove curvature radius	mm (in.)
r	Radius to raceway contact in tapered roller bearing	mm (in.)
r_f	Radius from inner-ring axis to roller end–flange contact in tapered roller bearing	mm (in.)
R_f	Radius from tapered roller axis to roller end–flange contact	mm (in.)
$\Re$	Ring radius to neutral axis	mm (in.)
$\Re$	Radius of locus of raceway groove curvature centers	mm (in.)
s	Distance between loci of inner and outer raceway groove curvature centers	mm (in.)
u	Ring radial deflection	mm (in.)
U	Strain energy	N × mm (lb × in.)
Z	Number of balls or rollers per bearing row	
α	Mounted contact angle	rad, °
α^o	Free contact angle	rad, °
β	$\tan^{-1} l/(d_m - D)$	rad, °
γ	$D\cos\alpha/d_m$	
δ	Deflection or contact deformation	mm (in.)
δ_1	Distance between inner and outer rings	mm (in.)
Δ	Contact deformation due to ideal normal loading	mm (in.)
$\Delta\psi$	Angular spacing between rolling elements	rad, °
ζ	Roller tilt angle	rad, °
η	$\tan^{-1} l/D$	rad, °
θ	Bearing misalignment angle	rad, °
λ	Lamina position	
μ	Coefficient of sliding friction between roller end and ring flange	
σ	Normal contact stress or pressure	MPa (psi)
ξ	Poisson's ratio	
ξ	Roller skewing angle	rad, °

1.1 GENERAL

In most bearing applications, only applied radial, axial, or combined radial and axial loadings are considered. However, under very heavy applied loading or if shafting is hollow to minimize weight, the shaft on which the bearing is mounted may bend, causing a significant moment load on the bearing. Also, the bearing housing may be nonrigid due to design targeted at minimizing both size and weight, causing it to bend while accommodating moment loading. Such combined radial, axial, and moment loadings result in altered distribution of load among the bearing's rolling element complement. This may cause significant changes in bearing deflections, contact stresses, and fatigue endurance compared to these operating parameters associated with the simpler load distributions considered in Chapter 7 of the first volume of this handbook.

In cylindrical and tapered roller bearings, the moment loading caused by bending of the shaft results in nonuniform load per unit length along the roller–raceway contacts. Misalignment of the bearing inner ring on the shaft or outer ring in the housing also generates moment loading in the bearing, causing a nonuniform load per unit length along the roller–raceway contacts. Thus, the maximum roller–raceway contact stresses will be greater than those occurring if the contacts are loaded uniformly along their lengths. Moreover, when bearing rings are misaligned, thrust loading is induced in the rollers, causing the rollers to tilt, further exacerbating the nonuniform roller–raceway contact loading. As seen in Chapter 11 in the first volume of this

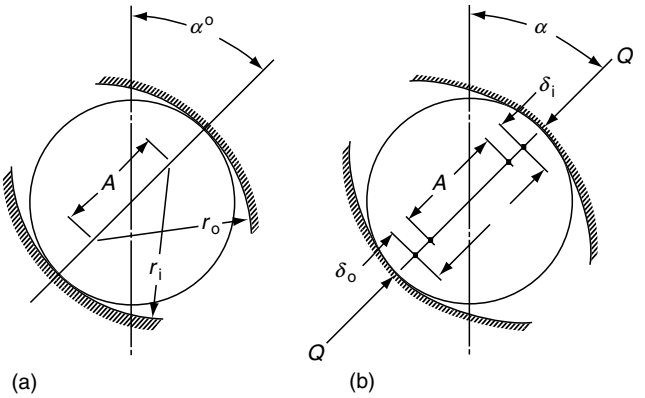

FIGURE 1.1 (a) Ball–raceway contact before applying load; (b) ball–raceway contact after load is applied.

handbook, fatigue life is inversely proportional to approximately the ninth power of contact stress. Hence, a nonuniform roller–raceway contact loading can result in significant reduction in bearing endurance.

In this chapter, methods to determine the distribution of applied loading among the rolling elements will be established considering each of the aforementioned effects.

1.2 BALL BEARINGS UNDER COMBINED RADIAL, THRUST, AND MOMENT LOADS

When a ball is compressed by load Q, since the centers of curvature of the raceway grooves are fixed with respect to the corresponding raceways, the distance between the centers is increased by the amount of the normal approach between the raceways. From Figure 1.1, it can be seen that

$$s = A + \delta_i + \delta_o \tag{1.1}$$

$$\delta_n = \delta_i + \delta_o = s - A \tag{1.2}$$

If a ball bearing that has a number of balls situated symmetrically about a pitch circle is subjected to a combination of radial, thrust (axial), and moment loads, the following relative displacements of inner and outer raceways may be defined:

δ_a Relative axial displacement
δ_r Relative radial displacement
θ Relative angular displacement

These relative displacements are shown in Figure 1.2.

Consider a rolling bearing before the application of a load. Figure 1.3 shows the positions of the loci of the centers of the inner and outer raceway groove curvature radii. It can be determined from Figure 1.4 that the locus of the centers of the inner-ring raceway groove curvature radii is expressed by

$$\Re_i = \frac{d_m}{2} + \left(r_i - \frac{D}{2}\right)\cos\alpha^o \tag{1.3}$$

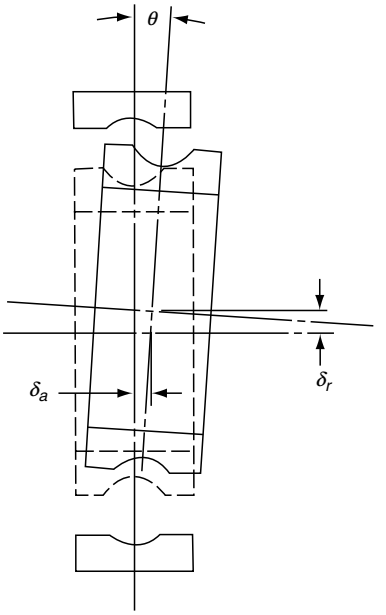

FIGURE 1.2 Displacements of an inner ring (outer ring fixed) due to application of combined radial, axial, and moment loadings.

where α^{o} is the free contact angle determined by bearing diametral clearance. From Figure 1.3 then

$$\Re_{o} = \Re_{i} - A\cos\alpha^{o} \tag{1.4}$$

$$\Re_{i} - \Re_{o} = A\cos\alpha^{o} \tag{1.5}$$

In Figure 1.3, ψ is the angle between the most heavily loaded rolling element and any other rolling element. Because of symmetry $0 \leq \psi \leq \pi$.

If the outer ring of the bearing is considered fixed in space as the load is applied to the bearing, then the inner ring will be displaced and the locus of inner-ring raceway groove radii centers will also be displaced as shown in Figure 1.5. From Figure 1.5 it can be determined that s, the distance between the centers of curvature of the inner- and outer-ring raceway grooves at any rolling element position ψ, is given by

$$s = \left[\left(A\sin\alpha^{o} + \delta_{a} + \Re_{i}\,\theta\cos\psi\right)^{2} + \left(A\cos\alpha^{o} + \delta_{r}\cos\psi\right)^{2}\right]^{1/2} \tag{1.6}$$

or

$$s = A\left[\left(\sin\alpha^{o} + \overline{\delta}_{a} + \Re_{i}\,\overline{\theta}\cos\psi\right)^{2} + \left(\cos\alpha^{o} + \overline{\delta}_{r}\cos\psi\right)^{2}\right]^{1/2} \tag{1.7}$$

where

$$\overline{\delta}_{a} = \frac{\delta_{a}}{A} \tag{1.8}$$

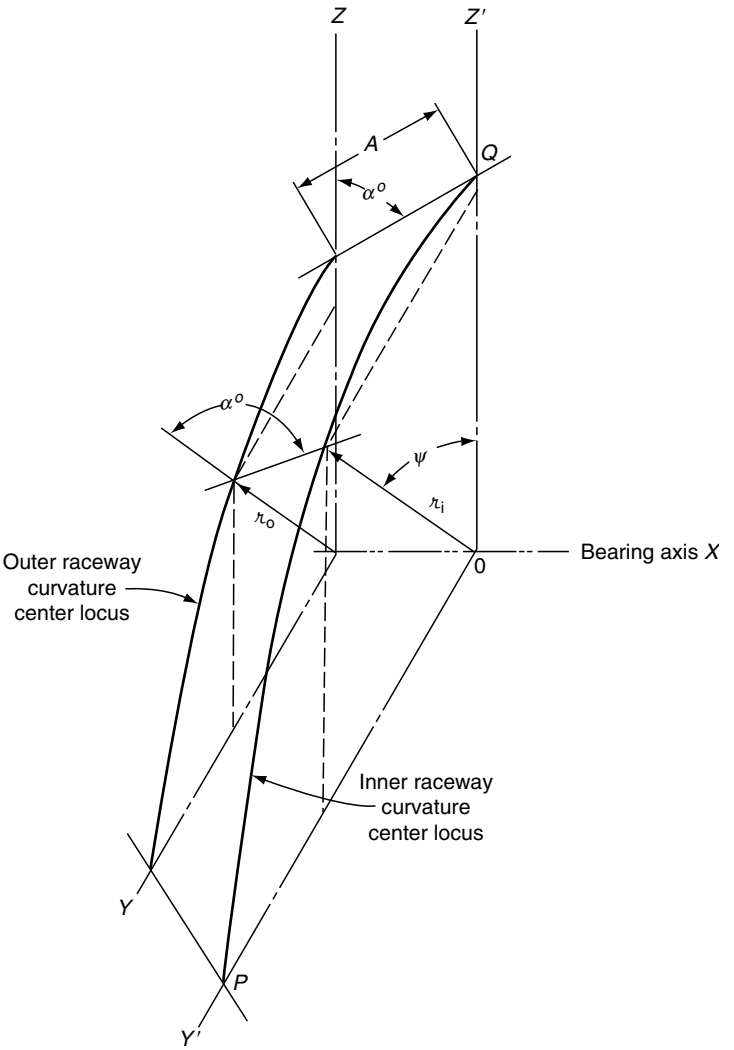

FIGURE 1.3 Loci of raceway groove curvature radii centers before applying load. (From Jones, A., *Analysis of Stresses and Deflections*, New Departure Engineering Data, Bristol, CT, 1946.)

$$\overline{\delta}_{\mathrm{r}} = \frac{\delta_{\mathrm{r}}}{A} \tag{1.9}$$

$$\overline{\theta} = \frac{\theta}{A} \tag{1.10}$$

Substituting Equation 1.7 into Equation 1.2 yields

$$\delta_{\mathrm{n}} = A\left\{\left[\left(\sin\alpha^{\mathrm{o}} + \overline{\delta}_{\mathrm{a}} + \Re_{\mathrm{i}}\,\overline{\theta}\cos\psi\right)^2 + \left(\cos\alpha^{\mathrm{o}} + \overline{\delta}_{\mathrm{r}}\cos\psi\right)^2\right]^{1/2} - 1\right\} \tag{1.11}$$

From Chapter 7 of the first volume of this book, the load vs. deformation relationship for a rolling element–raceway contact is given by

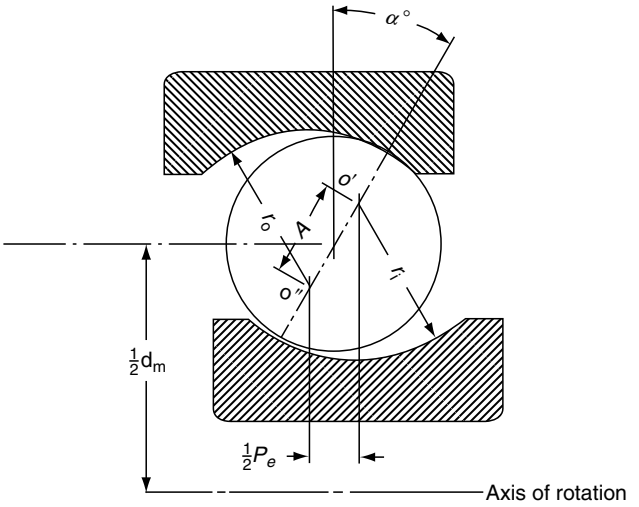

FIGURE 1.4 Radial ball bearing showing ball–raceway contact due to axial shift of inner and outer rings.

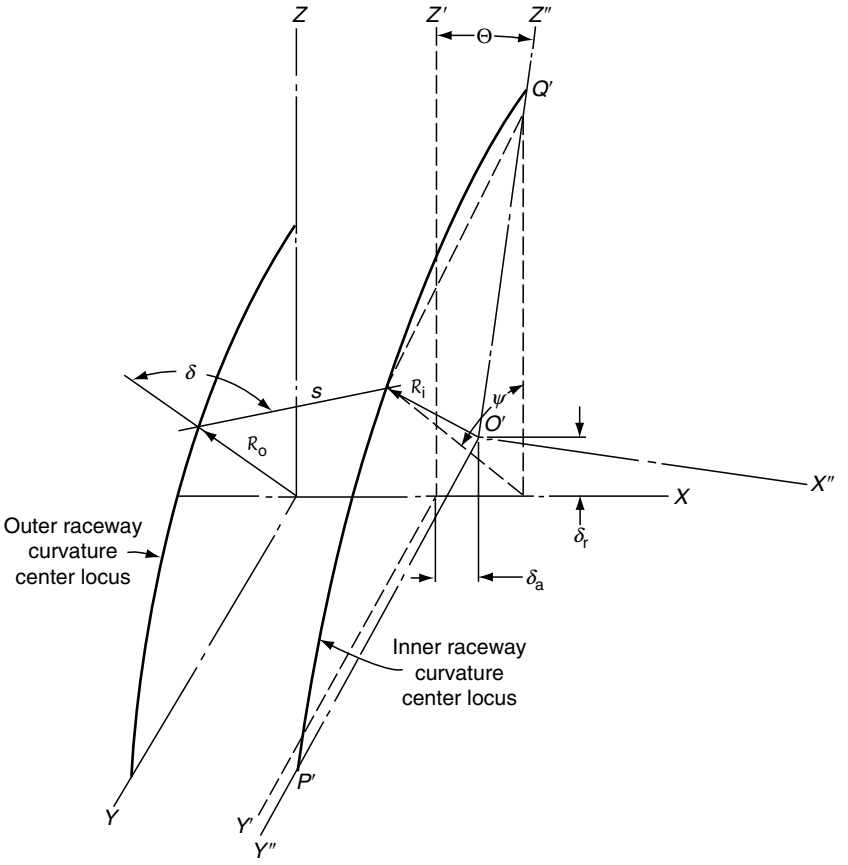

FIGURE 1.5 Loci of raceway groove curvature radii centers after displacement (From Jones, A., *Analysis of Stresses and Deflections*, New Departure Engineering Data, Bristol, CT, 1946.)

$$Q = K_{\mathrm{n}}\delta^{n} \tag{1.12}$$

In Equation 1.12, exponent $n = 3/2$ for ball bearings and 10/9 for roller bearings. Substitution of Equation 1.11 into Equation 1.12 and using the former exponent gives

$$Q = K_{\mathrm{n}}A^{1.5}\left\{\left[\left(\sin\alpha^{\mathrm{o}} + \overline{\delta}_{\mathrm{a}} + \Re_{\mathrm{i}}\,\overline{\theta}\cos\psi\right)^{2} + \left(\cos\alpha^{\mathrm{o}} + \overline{\delta}_{\mathrm{r}}\cos\psi\right)^{2}\right]^{1/2} - 1\right\}^{1.5} \tag{1.13}$$

At any ball azimuth position ψ, the operating contact angle is α. This angle can be determined from

$$\sin\alpha = \frac{\sin\alpha^{\mathrm{o}} + \overline{\delta}_{\mathrm{a}} + \Re_{\mathrm{i}}\,\overline{\theta}\cos\psi}{\left[\left(\sin\alpha^{\mathrm{o}} + \overline{\delta}_{\mathrm{a}} + \Re_{\mathrm{i}}\,\overline{\theta}\cos\psi\right)^{2} + \left(\cos\alpha^{\mathrm{o}} + \overline{\delta}_{\mathrm{r}}\cos\psi\right)^{2}\right]^{1/2}} \tag{1.14}$$

or

$$\cos\alpha = \frac{\cos\alpha^{\mathrm{o}} + \overline{\delta}_{\mathrm{r}}\cos\psi}{\left[\left(\sin\alpha^{\mathrm{o}} + \overline{\delta}_{\mathrm{a}} + \Re_{\mathrm{i}}\,\overline{\theta}\cos\psi\right)^{2} + \left(\cos\alpha^{\mathrm{o}} + \overline{\delta}_{\mathrm{r}}\cos\psi\right)^{2}\right]^{1/2}} \tag{1.15}$$

Equation 1.12 describes the normal load on the raceway acting through the contact angle. This normal load may be resolved into axial and radial components as follows:

$$Q_{\mathrm{a}} = Q\sin\alpha \tag{1.16}$$

$$Q_{\mathrm{r}} = Q\cos\psi\cos\alpha \tag{1.17}$$

If the radial and thrust loads applied to the bearing are F_{r} and F_{a}, respectively, then for static equilibrium to exist

$$F_{\mathrm{a}} = \sum_{\psi=0}^{\psi=\pm\pi} Q_{\psi}\sin\alpha \tag{1.18}$$

$$F_{\mathrm{r}} = \sum_{\psi=0}^{\psi=\pm\pi} Q_{\psi}\cos\psi\cos\alpha \tag{1.19}$$

Additionally, each of the thrust components produce a moment about the Y-axis such that

$$M_{\psi} = \frac{d_{\mathrm{m}}}{2}Q_{\psi}\cos\psi\sin\alpha \tag{1.20}$$

For static equilibrium, the applied moment M about the Y-axis must equal the sum of the moments of each rolling element about the Y-axis (in the case of load symmetry, rolling element thrust component moments about the Z-axis are self-equilibrating).

$$M = \frac{d_{\mathrm{m}}}{2}\sum_{\psi=0}^{\psi=\pm\pi} Q_{\psi}\cos\psi\sin\alpha \tag{1.21}$$

Combining Equation 1.13, Equation 1.16, and Equation 1.18 yields

$$F_a - K_n A^{1.5} \sum_{\psi=0}^{\psi=\pm\pi} \frac{\left\{\left[\left(\sin\alpha^o + \overline{\delta}_a + \Re_i\,\overline{\theta}\cos\psi\right)^2 + \left(\cos\alpha^o + \overline{\delta}_r\cos\psi\right)^2\right]^{1/2} - 1\right\}^{1.5}\left(\sin\alpha^o + \overline{\delta}_a + \Re_i\,\overline{\theta}\cos\psi\right)}{\left[\left(\sin\alpha^o + \overline{\delta}_a + \Re_i\,\overline{\theta}\cos\psi\right)^2 + \left(\cos\alpha^o + \overline{\delta}_r\cos\psi\right)^2\right]^{1/2}} = 0 \tag{1.22}$$

$$F_r - K_n A^{1.5} \sum_{\psi=0}^{\psi=\pm\pi} \frac{\left\{\left[\left(\sin\alpha^o + \overline{\delta}_a + \Re_i\,\overline{\theta}\cos\psi\right)^2 + \left(\cos\alpha^o + \overline{\delta}_r\cos\psi\right)^2\right]^{1/2} - 1\right\}^{1.5}\left(\cos\alpha^o + \overline{\delta}_r\cos\psi\right)\cos\psi}{\left[\left(\sin\alpha^o + \overline{\delta}_a + \Re_i\,\overline{\theta}\cos\psi\right)^2 + \left(\cos\alpha^o + \overline{\delta}_r\cos\psi\right)^2\right]^{1/2}} = 0 \tag{1.23}$$

$$M - \frac{d_m}{2} K_n A^{1.5} \sum_{\psi=0}^{\psi=\pm\pi} \frac{\left\{\left[\left(\sin\alpha^o + \overline{\delta}_a + \Re_i\,\overline{\theta}\cos\psi\right)^2 + \left(\cos\alpha^o + \overline{\delta}_r\cos\psi\right)^2\right]^{1/2} - 1\right\}^{1.5}\left(\sin\alpha^o + \overline{\delta}_a + \Re_i\,\overline{\theta}\cos\psi\right)\cos\psi}{\left[\left(\sin\alpha^o + \overline{\delta}_a + \Re_i\,\overline{\theta}\cos\psi\right)^2 + \left(\cos\alpha^o + \overline{\delta}_r\cos\psi\right)^2\right]^{1/2}} = 0 \tag{1.24}$$

These equations were developed by Jones [1].

Equation 1.22 through Equation 1.24 are simultaneous nonlinear equations with unknowns δ_a, δ_r, and θ. They may be solved by numerical methods; for example, the Newton–Raphson method. Having obtained δ_a, δ_r, and θ, the maximum ball load may be obtained from Equation 1.13 for $\psi = 0$.

$$Q_{max} = K_n A^{1.5}\left\{\left[\left(\sin\alpha^o + \overline{\delta}_a + \Re_i\,\overline{\theta}\right)^2 + \left(\cos\alpha^o + \overline{\delta}_r\right)^2\right]^{1/2} - 1\right\}^{1.5} \tag{1.25}$$

Solution of the indicated equations generally necessitates the use of a digital computer.

1.3 MISALIGNMENT OF RADIAL ROLLER BEARINGS

Although it is undesirable, radial cylindrical roller bearings and tapered roller bearings can support to a small extent the moment loading due to misalignment. The various types of misalignment are illustrated in Figure 1.6. Spherical roller bearings are designed to exclude moment loads from acting on the bearings and therefore are not included in this discussion. Figure 1.7 illustrates the misalignment of the inner ring of a cylindrical roller bearing relative to the outer ring.

To commence the analysis, it is assumed that any roller–raceway contact can be divided into a number of "slices" or laminae situated in planes parallel to the radial plane of the bearing. It is also assumed that shear effects between these laminae can be neglected owing to the small magnitudes of the contact deformations that develop. (Only contact deformations are considered.)

1.3.1 Components of Deformation

In a misaligned cylindrical roller bearing subjected to radial load, at each lamina in a crowned roller–raceway contact, the deformation may be considered to be composed of three components: (1) Δ_{mj} due to the radial load at the roller azimuth location j, (2) c_λ due to the crown drop at lamina λ, and (3) the deformation due to bearing misalignment and

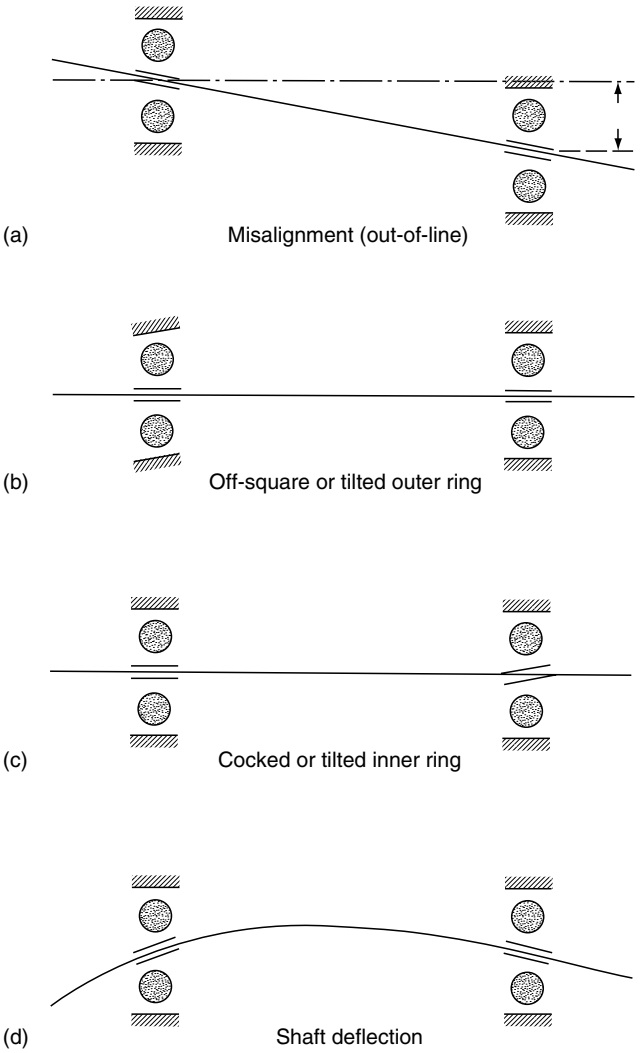

FIGURE 1.6 Types of misalignments.

roller tilt at the roller azimuth location *j*. These components are shown schematically in Figure 1.8.

The component due to radial load is the only contact deformation component considered in the simplified analytical methods presented in Chapter 7 of the first volume of this book. It needs no further explanation here.

1.3.1.1 Crowning

As stated previously, crowning of rollers and raceways is accomplished to avoid edge loading that can result in early fatigue failure of the rolling components. It may be accomplished in various forms. The simplest of these is the full circular profile crown illustrated in Figure 1.9. The rollers in most spherical roller bearings may be considered fully crowned whether of symmetrical contour (barrel-shaped) or of asymmetrical contour. In the latter case, the crown is offset from the roller mid-length point. Full crowning may also be applied to raceways as

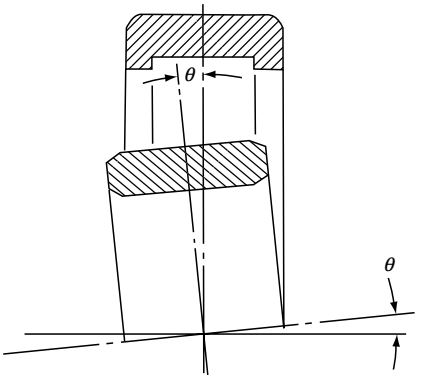

FIGURE 1.7 Misalignment of cylindrical roller bearing rings.

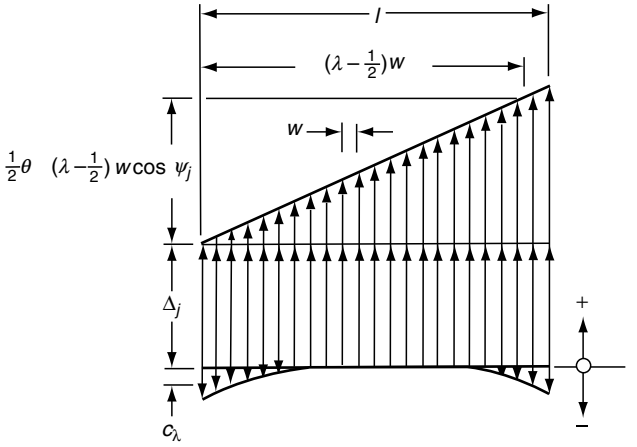

FIGURE 1.8 Components of roller–raceway contact deformation due to radial load, misalignment, and crowning.

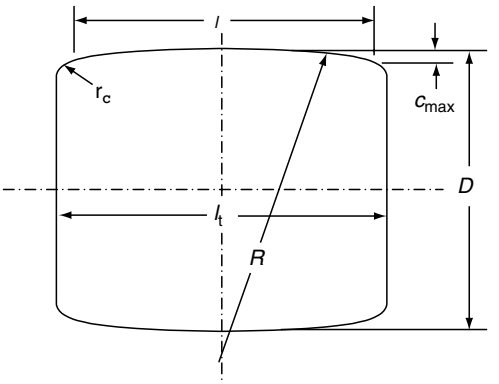

FIGURE 1.9 Schematic diagram of cylindrical roller with full circular profile crown.

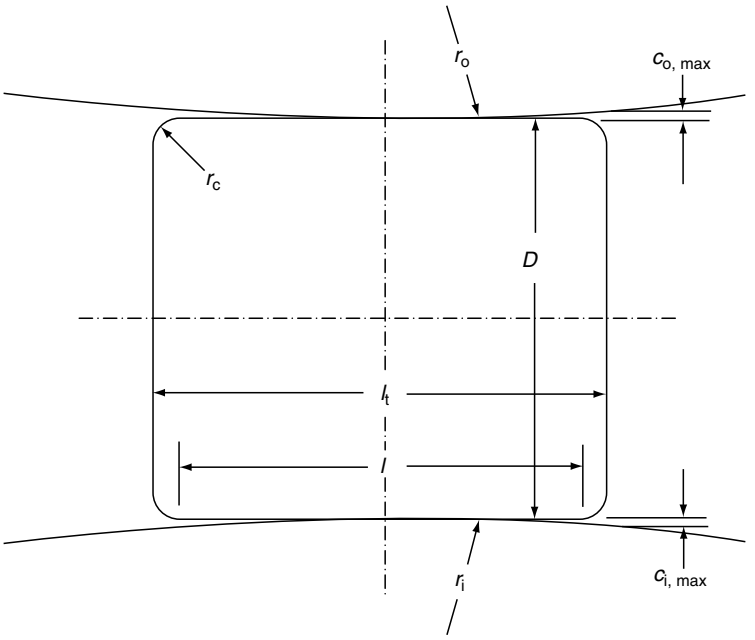

FIGURE 1.10 Schematic diagram of uncrowned (straight profile) cylindrical roller contacting inner and outer raceways, each with a full circular profile crown.

shown in Figure 1.10. This is commonly used in tapered roller bearings where often both the cone and cup raceways are crowned, and the rollers are not crowned.

Most cylindrical roller bearings employ rollers that are crowned only over a portion of the roller contour; the remaining portion is cylindrical (the contour is sometimes called flat or straight). A partially crowned cylindrical roller is illustrated in Figure 1.11.

From Figure 1.8, it can be seen that crown drop or crown gap c_λ at a selected lamina is considered as a negative deformation; that is, no roller–raceway loading can occur at a lamina until c_λ is overcome by the radial or the misalignment deformation. For both the fully crowned or partially crowned rollers that have circular profiles, Equation 1.26 defines c_λ in terms of the roller and crown dimensions, where $1 \leq \lambda \leq k$.

$$c_\lambda = \begin{cases} c_{\max}\left[\dfrac{\left(\frac{2\lambda-1}{k}-1\right)^2-\left(\frac{l_s}{l}\right)^2}{1-\frac{l_s}{l}}\right] & \left(\dfrac{2\lambda-1}{k}-1\right)^2-\left(\dfrac{l_s}{l}\right)^2 > 0 \\ 0 & \left(\dfrac{2\lambda-1}{k}-1\right)^2-\left(\dfrac{l_s}{l}\right)^2 \leq 0 \end{cases} \tag{1.26}$$

For rollers with circular profile partial crowns, blending between the straight and crowned portions of the profile is necessary to minimize stress concentrations and the resulting reduced fatigue life. To avoid such stress concentrations, in lieu of a circular profile, a tangential profile might be used. In this case, the crown radius would be variable, and the crown gap at each lamina k would be calculated using

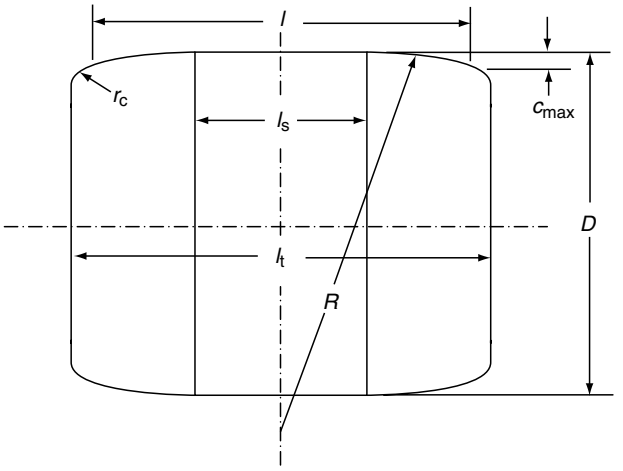

FIGURE 1.11 Schematic diagram of a partially crowned cylindrical roller.

$$c_\lambda = \begin{cases} c_{\max}\left[\dfrac{\left|\frac{2\lambda-1}{k}-1\right|-\frac{l_s}{l}}{1-\frac{l_s}{l}}\right]^2 & \left|\frac{2\lambda-1}{k}-1\right|-\frac{l_s}{l}>0 \\ 0 & \left|\frac{2\lambda-1}{k}-1\right|-\frac{l_s}{l}\le 0 \end{cases} \tag{1.27}$$

To minimize edge loading, Lundberg and sjövall [2] devised a fully crowned roller having a logarithmic profile. The crown gap at each lamina k is calculated using

$$c_\lambda = 0.2 \cdot ln\left[\frac{1}{1.0067-\left(\dfrac{2\lambda-1}{k}-1\right)^2}\right] \tag{1.28}$$

Subsequently, Reussner [3] developed another logarithmic profile crown believed to be more effective. The crown gap at each lamina k for the Reussner crown profile is given by

$$c_\lambda = 2\times 10^{-4}\Sigma\rho w^2 k^2 \cdot \ln\left[\frac{1}{1-\left(\dfrac{2\lambda-1}{k}-1\right)^6}\right] \tag{1.29}$$

It is possible to combine roller crowning and raceway crowning. In this case, the crown gap at each lamina k would be calculated as the sum of the crown gaps for the roller and raceway as follows:

$$c_{m\lambda} = c_{R\lambda} + c_{m\lambda} \tag{1.30}$$

In the above equation, subscript R refers to the roller and m to the raceway (m = i or m = o).

For the bearing misalignment θ shown in Figure 1.7, the effective misalignment at the azimuth location of the roller ψ_j is $\pm 1/2\theta \cos \psi_j$. The plus sign pertains to $0 \le \psi_j \le \pi/2$; the

minus sign pertains to $\pi/2 \leq \psi_j \leq \pi$ (assuming symmetry of loading about the 0–π diameter). Therefore, the total roller–raceway deformation at roller location j and lamina λ is given by

$$\delta_{\lambda j} = \Delta_j \pm \frac{\theta}{2}\left(\lambda - \frac{1}{2}\right) w \cos\psi_j - c_\lambda \tag{1.31}$$

1.3.2 Load on a Roller–Raceway Contact Lamina

In Chapter 6 of the first volume of this book, the following equations were given to describe the deformation vs. load for a roller–raceway contact:

$$\delta = \frac{2Q(1-\xi^2)}{\pi El} \ln\left[\frac{\pi El^2}{Q(1-\xi^2)(1 \mp \gamma)}\right] \tag{1.32}$$

$$\delta = 3.84 \times 10^{-5} \frac{Q^{0.9}}{l^{0.8}} \tag{1.33}$$

Equation 1.32 was developed by Lundberg and Sjövall [2] for an ideal line contact. In Equation 1.32, $\gamma = D \cos\alpha/d_m$, E is the modulus of elasticity, and ξ is Poisson's ratio. Equation 1.33 was developed empirically by Palmgren [4] from laboratory test data and pertains to the contact of a crowned roller on a raceway. While the load–deformation characteristic of an individual contact lamina may be described using either equation, the latter is applied here as the solution of a transcendental equation leads to force and moment equilibrium equations of greater complexity. Considering that the contact is divided into k laminae, each lamina of width w, the contact length is kw. Letting $q = Q/l$, Equation 1.33 becomes

$$\delta = 3.84 \times 10^{-5} q^{0.9} (kw)^{0.1} \tag{1.34}$$

Rearranging the above equation to define q yields

$$q = \frac{\delta^{1.11}}{1.24 \times 10^{-5} \ (kw)^{0.11}} \tag{1.35}$$

Equation 1.35 does not consider edge stresses; however, because these obtain only over very small areas, they can be neglected with little loss of accuracy when considering equilibrium of loading. Substitution of Equation 1.31 into Equation 1.35 gives

$$q_{\lambda j} = \frac{\left[\Delta_j \pm \theta\left(\lambda - \frac{1}{2}\right) w \cos\psi_j - c_\lambda\right]^{1.11}}{1.24 \times 10^{-5} (k_j w)^{0.11}} \tag{1.36}$$

Depending on the degree of loading and misalignment, all laminae in every contact may not be loaded; in Equation 1.36, k_j is the number of laminae under load at roller location j. Total roller loading is given by

$$Q_j = \frac{w^{0.89}}{1.24 \ \times \ 10^{-5} k_j^{0.11}} \sum_{\lambda=1}^{\lambda=k_j} \left[\Delta_j \ \pm \frac{1}{2}\theta\left(\lambda - \frac{1}{2}\right) w \cos\psi_j - c_\lambda\right]^{1.11} \tag{1.37}$$

1.3.3 Equations of Static Equilibrium

To determine the individual roller loading, it is necessary to satisfy the requirements of static equilibrium. Hence, for an applied radial load,

$$\frac{F_r}{2} - \sum_{j=1}^{j=Z/2+1} \tau_j Q_j \cos\psi_j = 0 \quad \begin{matrix} \tau_j = 0.5; & \psi_j = 0, \pi \\ \tau_j = 1; & \psi_j \neq 0, \pi \end{matrix} \tag{1.38}$$

Substituting Equation 1.37 into Equation 1.38 yields

$$\frac{0.62 \times 10^{-5} F_r}{w^{0.89}} - \sum_{j=1}^{j=Z/2+1} \frac{\tau_j \cos\psi_j}{k_j^{0.11}} \sum_{\lambda=1}^{\lambda=k_j} \left[\Delta_j \pm \frac{1}{2}\theta\left(\lambda - \frac{1}{2}\right) w \cos\psi_j - c_\lambda\right]^{1.11} = 0 \tag{1.39}$$

For an applied coplanar misaligning moment load, the equilibrium condition to be satisfied is

$$\frac{\mathfrak{M}}{2} - \sum_{j=1}^{j=Z/2+1} \tau_j Q_j e_j \cos\psi_j = 0 \quad \begin{matrix} \tau_j = 0.5; & \psi_j = 0, \pi \\ \tau_j = 1; & \psi_j \neq 0, \pi \end{matrix} \tag{1.40}$$

where e_j is the eccentricity of loading at each roller location. e_j, which is illustrated in Figure 1.12, is given by

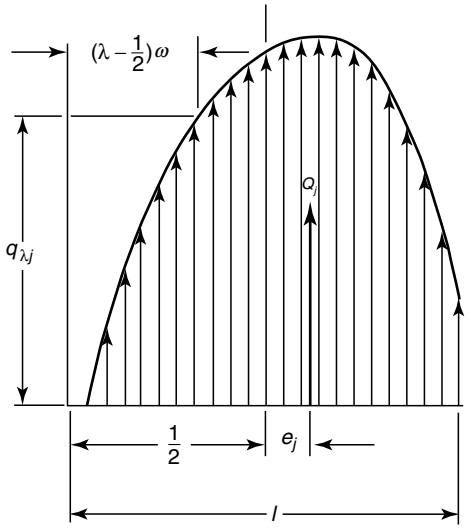

FIGURE 1.12 Load distribution for a misaligned crowned roller showing eccentricity of loading.

$$e_j = \frac{\sum_{\lambda=1}^{\lambda=k_j} q_{\lambda j}\left(\lambda - \frac{1}{2}\right)w}{\sum_{\lambda=1}^{\lambda=k_j} q_{\lambda j}} - \frac{l}{2} \quad j = 3, \qquad \frac{Z}{2} + 3 \tag{1.41}$$

Hence,

$$\frac{0.62 \times 10^{-5}\mathfrak{N}}{w^{0.89}} - \sum_{j=1}^{j=Z/2+1} \frac{\tau_j \cos\psi_j}{k_j^{0.11}} \times \left\{ \sum_{\lambda=1}^{\lambda=k_j} \left[\Delta_j \pm \frac{1}{2}\theta\left(\lambda - \frac{1}{2}\right)w\cos\psi_j - c_j \right]^{1.11} \left(\lambda - \frac{1}{2}\right)w - \frac{l}{2}\sum_{\lambda=1}^{\lambda=k_j} \left[\Delta_j \pm \frac{1}{2}\theta\left(\lambda - \frac{1}{2}\right)w\cos\psi_j - c_\lambda \right]^{1.11} \right\} = 0 \tag{1.42}$$

1.3.4 Deflection Equations

The remaining equations to be established are the radial deflection relationships. It is necessary here to determine the relative radial movement of the rings caused by the misalignment as well as that owing to radial loading. To assist in the first determination, Figure 1.13 shows schematically an inner ring–roller assembly misaligned with respect to the outer ring. From this sketch, it is evident that one half of the roller included angle is described by

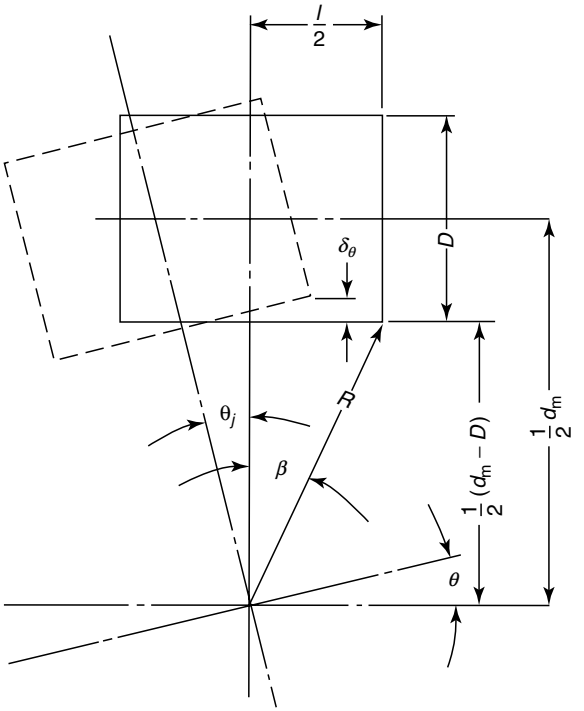

FIGURE 1.13 Schematic diagram of misaligned roller–inner ring assembly showing interference with outer ring.

$$\beta = \tan^{-1} \frac{l}{d_m - D} \tag{1.43}$$

and

$$\sin \beta = \frac{l}{[(d_m - D)^2 + l^2]^{1/2}} \tag{1.44}$$

The maximum radial interference between a roller and the outer ring owing to misalignment is given by

$$\delta_\theta = R \cos(\beta - \theta_j) - R \cos \beta \tag{1.45}$$

where

$$R = 0.5 \times [(d_m - D)^2 + l^2]^{1/2} \tag{1.46}$$

In developing Equation 1.45 and Equation 1.46, the effect of crown drop was investigated and found to be negligible.

Expanding Equation 1.46 in terms of the trigonometric identity further yields

$$\delta_\theta = R(\cos \beta \cos \theta_j + \sin \beta \sin \theta_j - \cos \beta) \tag{1.47}$$

As θ_j is small, $\cos \theta_j \to 1$, and $\sin \theta_j \to \theta_j$. Moreover, $\theta_j = \pm \theta \cos \psi_j$ and $\sin \beta = l/2R$; therefore,

$$\delta_\theta = \pm \tfrac{1}{2} l\theta \cos \psi_j \tag{1.48}$$

The shift of the inner-ring center relative to the outer-ring center owing to radial loading and clearance, and the subsequent relative radial movement at any roller location are shown in Figure 1.14. The sum of the relative radial movement of the rings at each roller angular location minus the clearance is equal to the sum of the inner and outer raceway maximum contact deformations at the same angular location. Stating this relationship in equation format:

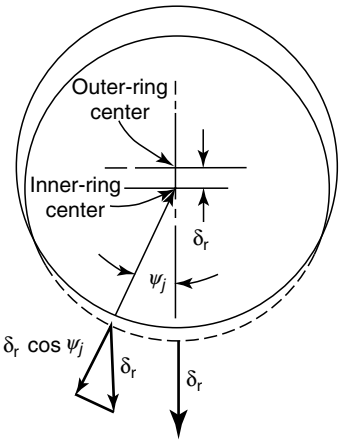

FIGURE 1.14 Displacement of ring centers caused by radial loading showing relative radial movement.

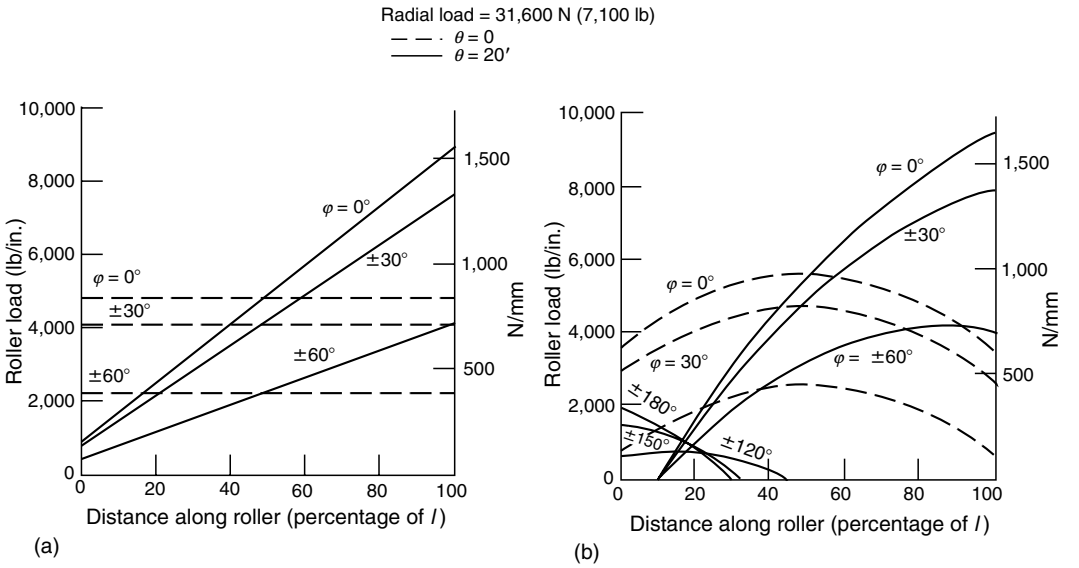

FIGURE 1.15 Roller loading vs. axial and circumferential location—309 cylindrical roller bearing: (a) ideally crowned rollers; (b) fully crowned rollers.

$$\left[\delta_r \pm \frac{1}{2} l\theta\right] \cos\psi_j - \frac{P_d}{2} - 2\left[\Delta_j \pm \frac{1}{2}\theta\left(\lambda - \frac{1}{2}\right) w \cos\psi_j - c_\lambda\right]_{\max} = 0 \qquad (1.49)$$

Equation 1.39, Equation 1.42, and Equation 1.49 constitute a set of $Z/2+3$ simultaneous nonlinear equations that can be solved for δ_r, θ, and Δ_j using numerical analysis techniques. Thereafter, the variation of roller load per unit length, and subsequently the roller load, may be determined for each roller location using Equation 1.36 and Equation 1.37, respectively.

Using this method of digital computation, Harris [5] analyzed a 309 cylindrical roller bearing having the following dimensions and loading:

Number of rollers	12
Roller effective length	12.6 mm (0.496 in.)
Roller straight lengths	4.78, 7.770, 12.6 mm
Roller crown radius	1,245 mm (49 in.)
Roller diameter	14 mm (0.551 in.)
Bearing pitch diameter	72.39 mm (2.85 in.)
Applied radial load	31,600 N (7,100 lb)

For these conditions, Figure 1.15 shows the loading on various rollers for the bearing with ideally crowned rollers ($l_s = 12.6$ mm [0.496 in.]) and with fully crowned rollers ($l_s = 0$).

Figure 1.16 shows the effect of roller crowning on bearing radial deflection as a function of misalignment.

1.4 THRUST LOADING OF RADIAL CYLINDRICAL ROLLER BEARINGS

When radial cylindrical roller bearings have fixed flanges on both inner and outer rings, they can carry some thrust load in addition to radial load. The greater the amount of radial load applied, the more is the thrust load that can be carried. As shown by Harris [6] and seen in Figure 1.17, the thrust load causes each roller to tilt an amount ζ_j.

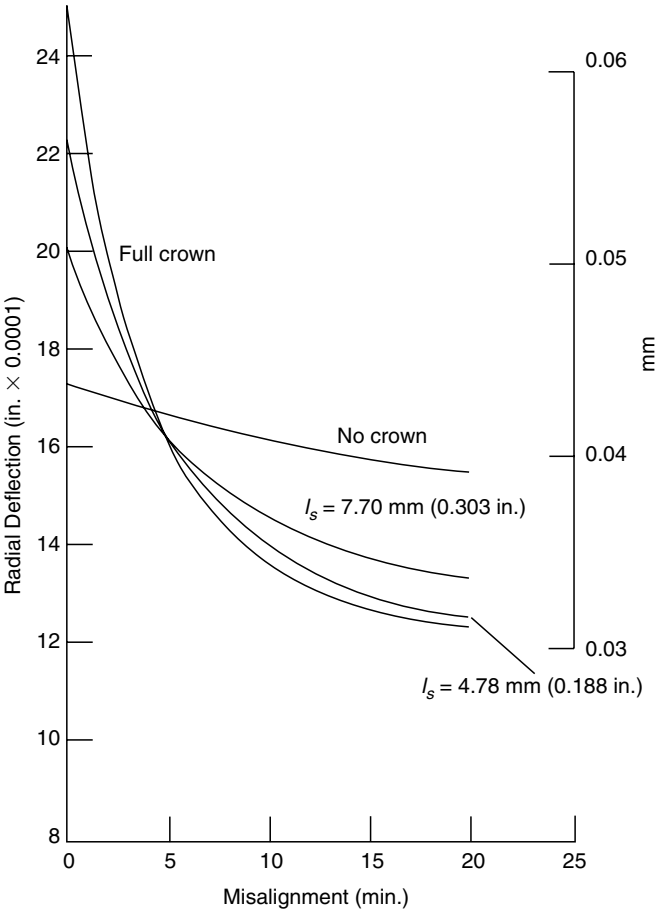

FIGURE 1.16 Roller deflection vs. misalignment and crowning—309 cylindrical roller bearing at 31,600 N (7,100 lb) radial load.

Again, it is assumed that a roller–raceway contact can be subdivided into laminae in planes parallel to the radial plane of the bearing. When a radial cylindrical roller bearing is subjected to applied thrust load, the inner ring shifts axially relative to the outer ring.

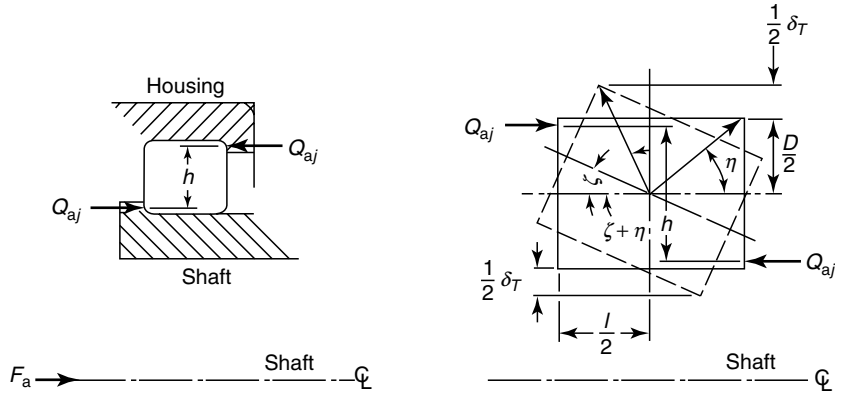

FIGURE 1.17 Thrust couple, roller tilting, and interference owing to applied thrust load.

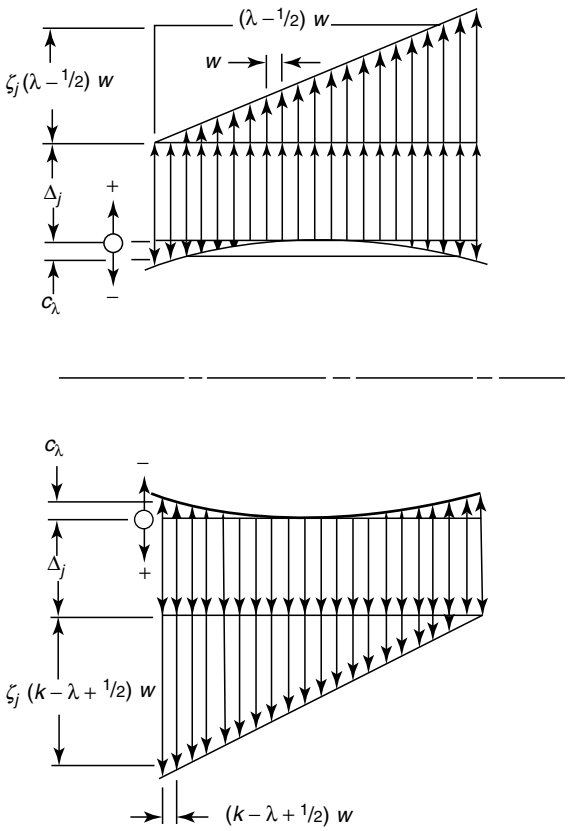

FIGURE 1.18 Components of roller–raceway deflection at opposing raceways due to radial load, thrust load, and crowning.

Assuming deflections owing to roller end–flange contacts are negligible, the interference at any axial location (lamina) is

$$\delta_{\lambda j} = \Delta_j + \zeta_j\left(\lambda - \frac{1}{2}\right)w - c_\lambda, \quad \lambda = 1, k_j \tag{1.50}$$

where c_λ is given by Equation 1.26 through Equation 1.30. Figure 1.18 illustrates the component deflections in Equation 1.50. Substituting Equation 1.50 into Equation 1.35 yields

$$q_{\lambda j} = \frac{\left[\Delta_j + \zeta_j\left(\lambda - \frac{1}{2}\right)w - c_\lambda\right]^{1.11}}{1.24 \times 10^{-5}(k_j w)^{0.11}} \tag{1.51}$$

and at any azimuth ψ_j, the total roller loading is

$$Q_j = \frac{w^{0.89}}{1.24 \times 10^{-5} k_j^{0.11}} \sum_{\lambda=1}^{\lambda=k_j} \left[\Delta_j + \zeta_j\left(\lambda - \frac{1}{2}\right)w - c_\lambda\right]^{1.11} \tag{1.52}$$

1.4.1 Equilibrium Equations

To determine roller loading, it is necessary to satisfy static equilibrium requirements. Hence, for applied radial load

$$\frac{F_r}{2} - \sum_{j=1}^{j=Z/2+1} \tau_j Q_j \cos\psi_j = 0 \quad \begin{matrix} \tau_j = 0.5; & \psi_j = 0, \pi \\ \tau_j = 1; & \psi_j \neq 0, \pi \end{matrix} \tag{1.53}$$

Substituting Equation 1.52 into Equation 1.53 yields

$$\frac{0.62 \times 10^{-5} F_r}{w^{0.89}} - \sum_{j=1}^{j=Z/2+1} \frac{\tau_j \cos\psi_j}{k_j^{0.11}} \sum_{\lambda=1}^{\lambda=k_j} \left[\Delta_j + \zeta_j\left(\lambda - \frac{1}{2}\right)w - c_\lambda\right]^{1.11} = 0 \tag{1.54}$$

For an applied centric thrust load, the equilibrium condition to be satisfied is

$$\frac{F_a}{2} - \sum_{j=1}^{j=Z/2+1} \tau_j Q_{aj} = 0 \tag{1.55}$$

At each roller location, the thrust couple is balanced by a radial load couple caused by the skewed axial load distribution. Thus, $hQ_{aj} = 2Q_j e_j$ and

$$\frac{F_a}{2} - \frac{2}{h} \sum_{j=1}^{j=Z/2+1} \tau_j Q_j e_j = 0 \quad \begin{matrix} \tau_j = 0.5; & \psi_j = 0, & \pi \\ \tau_j = 1; & \psi_j \neq 0, & \pi \end{matrix} \tag{1.56}$$

where e_j is the eccentricity of loading indicated in Figure 1.12 and defined by

$$e_j = \frac{\sum_{\lambda=1}^{\lambda=k_j} q_{\lambda j}\left(\lambda - \frac{1}{2}\right)w}{\sum_{\lambda=1}^{\lambda=k_j} q_{\lambda j}} - \frac{l}{2} \tag{1.57}$$

Substitution of Equation 1.52 and Equation 1.57 into Equation 1.56 yields

$$\begin{aligned} &\frac{0.31 \times 10^{-5} F_a}{w^{0.89}} - \sum_{j=1}^{j=Z/2+1} \frac{\tau_j}{k_j^{0.11}} \\ &\quad \times \left\{ \sum_{\lambda=1}^{\lambda=k_j} \left[\Delta_j \pm \zeta_j\left(\lambda - \frac{1}{2}\right)w - c_\lambda\right]^{1.11} \left(\lambda - \frac{1}{2}\right)w - \frac{l}{2} \right. \\ &\quad \left. \times \sum_{\lambda=1}^{\lambda=k_j} \left[\Delta_j \pm \zeta_j\left(\lambda - \frac{1}{2}\right)w - c_\lambda\right]^{1.11} \right\} = 0 \quad \begin{matrix} \tau_j = \frac{1}{2}; & \psi_j = 0, \pi \\ \tau_j = 1; & \psi_j \neq 0, \pi \end{matrix} \end{aligned} \tag{1.58}$$

1.4.2 Deflection Equations

Radial deflection relationships remain to be established. It is necessary to determine the relative radial movement of the bearing rings caused by the thrust loading as well as that due to radial loading. To assist in this derivation, Figure 1.17 shows schematically a thrust-loaded roller–ring assembly. From this sketch, a roller angle is described by

$$\tan \eta = \frac{D}{l} \tag{1.59}$$

The maximum radial interference between a roller and both rings is given by

$$\delta_j = D\left[\frac{\sin(\zeta_j + \eta)}{\sin \eta} - 1\right] \tag{1.60}$$

In developing the above equation, the effect of crown drop was found to be negligible. Expanding Equation 1.60 in terms of the trigonometric identity and recognizing that ζ_j is small and $l = D\,\mathrm{ctn}\,\eta$ yields

$$\delta_{tj} = l\zeta_j \tag{1.61}$$

Although δ_{tj} is the radial deflection due to roller tilting, it can be similarly shown that axial deflection owing to roller tilting is

$$\delta_{aj} = D\zeta_j \tag{1.62}$$

Therefore, the radial interference caused by axial deflection is

$$\delta_{ra} = \delta_a \frac{l}{D} \tag{1.63}$$

The sum of the relative radial movements of the inner and outer rings at each roller azimuth minus the radial clearance is equal to the sum of the inner and outer raceway maximum contact deformations at the same azimuth, or

$$\delta_a \frac{l}{D} + \delta_r \cos \psi_j - \frac{P_d}{2} - 2\left[\Delta_j + \zeta_j\left(\lambda - \frac{1}{2}\right)w - c_\lambda\right]_{\max} = 0 \tag{1.64}$$

The set of simultaneous equations, Equation 1.54, Equation 1.58, and Equation 1.64, can be solved for ζ_j, Δ_j, δ_r, and δ_a. Thereafter, the variation of the roller load per unit length q and roller load Q may be determined for each roller azimuth using Equation 1.51 and Equation 1.52, respectively. The axial load on each roller may be determined from

$$Q_{aj} = \frac{w^{0.89}}{3.84 \times 10^{-5} k_j^{0.11} h} \times \left\{ \sum_{\lambda=1}^{\lambda=k_j} \left[\Delta_j + \zeta_j\left(\lambda - \frac{1}{2}\right)w - c_\lambda\right]^{1.11} \left(\lambda - \frac{1}{2}\right)w - \frac{l}{2} \sum_{\lambda=1}^{\lambda=k_j} \left[\Delta_j + \zeta_j\left(\lambda - \frac{1}{2}\right)w - c_\lambda\right]^{1.11} \right\} \tag{1.65}$$

1.4.3 Roller–Raceway Deformations Due to Skewing

When rollers are subjected to axial loading as shown in Figure 1.17, due to sliding motions between the roller ends and ring flanges, friction forces occur. For example, $F_{aj} = \mu Q_{aj}$, in which μ is the coefficient of friction. In a misaligned bearing, each roller that carries load is squeezed at one end and forced against the opposing flange with a load Q_{aj}, creating friction force F_{aj} at the roller end. Because of F_{aj}, a moment occurs creating, in addition to the predominant rolling motion about the roller axis, a yawing or skewing motion and secondary roller tilting. The tilting and skewing motions occur in orthogonal planes that contain the roller axis. Roller skewing is resisted by the concave curvature of the outer raceway. The resisting forces and accompanying deformations alter the distribution of load along both the outer and inner raceway–roller contacts. Figure 1.19 illustrates the forces that occur on a roller subjected to radial and thrust loadings. Frictional stresses $\sigma_{s1j\lambda}$ and $\sigma_{s2j\lambda}$ in Figure 1.19 tend not to significantly influence the roller–raceway normal loadings per unit length $q_{1j\lambda}$ and $q_{2j\lambda}$ on the outer and inner raceways, respectively.

Figure 1.20 shows the roller skewing angle ξ_j and the roller–outer raceway loading that result.

The roller–raceway contact deformations that result from skewing as demonstrated by Harris et al. [7] may be described by

$$\delta_{mj\lambda} = \Delta_{mj} + w\left(\lambda - \frac{1}{2}\right)\zeta_j + \phi_{mj\lambda} - c_\lambda \tag{1.66}$$

In the above equation, subscript m refers to the outer and inner raceway contacts; $m = 1$ and 2, respectively, and deformations due to skewing $\varphi_{mj\lambda}$ are given by

$$\phi_{1j\lambda} = \frac{\left[\left(\frac{k}{2} - \left|\lambda - \frac{1}{2}(k+1)\right|\right)w\right]}{d_m + D}\xi_j^2 \tag{1.67}$$

$$\phi_{2j\lambda} = \frac{\left[\left|\lambda - \frac{1}{2}(k+1)\right|w\right]^2}{d_m + D}\xi_j^2 \tag{1.68}$$

It can be further seen that Equation 1.64 must become

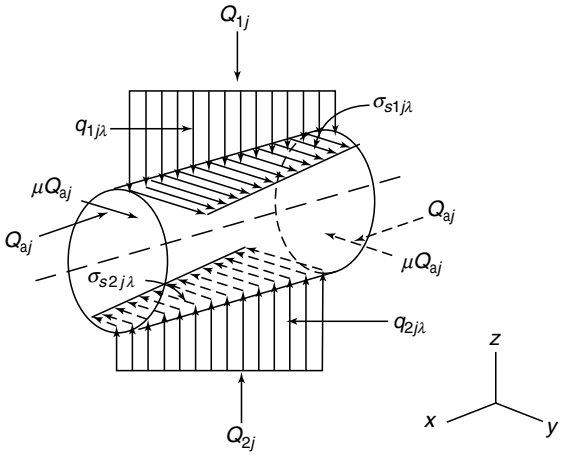

FIGURE 1.19 Normal and friction forces acting on a radial and thrust-loaded roller.

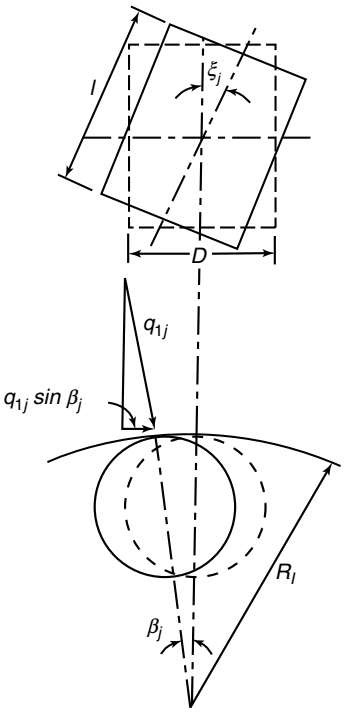

FIGURE 1.20 Roller–outer raceway contact showing roller skewing angle ξ_j and restoring forces.

$$\delta_a \frac{l}{D} + \delta_r \cos \psi_j - \frac{P_d}{2} - (\delta_{1mj,\,\max} + \delta_{2mj,\,\max}) = 0 \tag{1.69}$$

Owing to the unknown variables ξ_j and Δ_{mj}, the latter replacing Δ_j, additional equilibrium equations must be established. For equilibrium of roller loading in the radial direction,

$$\sum_{m=1}^{m=2} Q_{mj} = w \sum_{m=1}^{m=2} \sum_{\lambda=1}^{\lambda=k} q_{mj\lambda} = 0 \tag{1.70}$$

Referring to Figure 1.20 and considering equilibrium of moments in the plane of roller skewing,

$$\begin{aligned} lF_{aj} &+ \sum_{m=1}^{m=2} \sum_{\lambda=1}^{\lambda=k} w^2 \left[\lambda - \frac{1}{2}(k+1)\right] \sigma_{mj\lambda} \\ &- \sum_{m=1}^{m=2} \sum_{\lambda=1}^{\lambda=k} w^2 \left[\lambda - \frac{1}{2}(k+1)\right] q_{mj\lambda} \sin \beta_j = 0 \end{aligned} \tag{1.71}$$

As the angle $\beta_j \to 0$, $\sin \beta_j \to \beta_j$,

$$\sin \beta_j = \frac{2w}{d_m + D} \left[\lambda - \frac{1}{2}(k+1)\right] \xi_j \tag{1.72}$$

As indicated above, the frictional stresses, $\sigma_{s1j\lambda}$ and $\sigma_{s2j\lambda}$, tend not to influence the roller–raceway normal loading significantly, meaning that the frictional moment loading is rather small

compared with those caused by the restoring forces $q_{1j} \sin \beta_j$ shown in Figure 1.20 and roller end–flange friction forces. Therefore, substituting Equation 1.72 into Equation 1.71 yields

$$lF_{aj} - \frac{2w^3 \xi_j}{d_m + D} \sum_{m=1}^{m=2} \sum_{\lambda=1}^{\lambda=k} \left[\lambda - \frac{1}{2}(k+1)\right]^2 q_{mj\lambda} = 0 \tag{1.73}$$

Considering that the contact deformations due to roller radial loading are different for each roller–raceway contact, bearing load equilibrium equations, Equation 1.54 and Equation 1.58, must be changed accordingly; hence,

$$\frac{0.62 \times 10^{-5} F_r}{w^{0.89}} - \sum_{j=1}^{j=Z/2+1} \frac{\tau_j \cos \psi_j}{k_{2j}^{0.11}} \sum_{\lambda=1}^{\lambda=k} \left[\Delta_{2j} + w\left(\lambda - \frac{1}{2}\right)\zeta_j + \phi_{2j\lambda} - c_\lambda\right]^{1.11} = 0 \tag{1.74}$$

and

$$\frac{0.31 \times 10^{-5} F_a}{w^{0.89}} - \sum_{j=1}^{j=Z/2+1} \frac{\tau_j}{k_{2j}^{0.11}} \times \left\{ \sum_{\lambda=1}^{\lambda=k} \left[\Delta_{2j} + w\left(\lambda - \frac{1}{2}\right)\zeta_j + \phi_{2j\lambda} - c_\lambda\right]^{1.11} w\left(\lambda - \frac{1}{2}\right) - \frac{l}{2} \sum_{\lambda=1}^{\lambda=k} \left[\Delta_{2j} + w\left(\lambda - \frac{1}{2}\right)\zeta_j + \phi_{2j\lambda} - c_\lambda\right]^{1.11} \right\} = 0 \tag{1.75}$$

Equation 1.56, Equation 1.69, Equation 1.70, and Equation 1.73 through Equation 1.75 constitute a set of simultaneous, nonlinear equations that may be solved for Δ_{mj}, ζ_j, ξ_j, δ_r, and δ_a. Subsequently, the roller–raceway loads Q_j and roller end–flange loads Q_{aj} may be determined.

The skewing angles determined using the earlier equations strictly pertain to full complement bearings and bearings having no roller guide flanges. For a bearing with a substantially robust and rigid cage, the skewing angle may be limited by the clearances between the rollers and the cage pockets. For a bearing with guide flanges, the skewing may be limited by the endplay between the roller ends and guide flanges. In general, the latter situation is obtained; however, to the extent that skewing is permitted, the earlier analysis is applicable.

1.5 RADIAL, THRUST, AND MOMENT LOADINGS OF RADIAL ROLLER BEARINGS

1.5.1 Cylindrical Roller Bearings

For radial cylindrical roller bearings, it is possible to apply general combined loading. The equations for load equilibrium defined earlier apply; however, the interference at any lamina in the roller–raceway contact is given by

$$\delta_{mj\lambda} = \Delta_{mj} + w\left(\lambda - \frac{1}{2}\right)\left(v_m \zeta_j \pm \frac{1}{2}\theta \cos \psi_j\right) + \phi_{mj\lambda} - c_\lambda \tag{1.76}$$

where subscript $m = 1$ refers to the outer raceway and $m = 2$ refers to the inner raceway. Coefficient $v_1 = -1$ and $v_2 = +1$. The contact load per unit length is given by

$$q_{mj\lambda} = \frac{\left[\Delta_{mj} + w\left(\lambda - \frac{1}{2}\right)\left(\nu_m \zeta_j \pm \frac{1}{2}\theta \cos\psi_j\right) + \phi_{mj\lambda} - c_\lambda\right]^{1.11}}{1.24 \times 10^{-5}\left(k_j w\right)^{0.11}} \tag{1.77}$$

1.5.2 Tapered Roller Bearings

Similar equations may be developed for tapered roller bearings. As shown in Chapter 5 of the first volume of this book, roller end–flange loading occurs during all conditions of applied loading, and bearing equilibrium equations must be altered accordingly. Figure 1.21 illustrates the geometry and loading of a tapered roller in a bearing.

Considering Figure 1.21 and establishing the following dimensions:

r_2 Radius in a radial plane from the inner-ring axis of rotation to the center of the inner raceway contact
r_{fz} Radius in a radial plane from the inner-ring axis of rotation to the center of the roller end–inner ring flange contact
r_{fx} x Direction distance in an axial plane from the center of the inner raceway contact to the center of the roller end–inner ring flange contact

The roller load equilibrium equations are

$$w \sum_{m=1}^{m=2} c_m \cos\alpha_m \sum_{\lambda=1}^{\lambda=k} q_{mj\lambda} - Q_{fj} \cos\alpha_f = 0 \tag{1.78}$$

$$w \sum_{m=1}^{m=2} c_m \sin\alpha_m \sum_{\lambda=1}^{\lambda=k} q_{mj\lambda} + Q_{fj} \sin\alpha_f = 0 \tag{1.79}$$

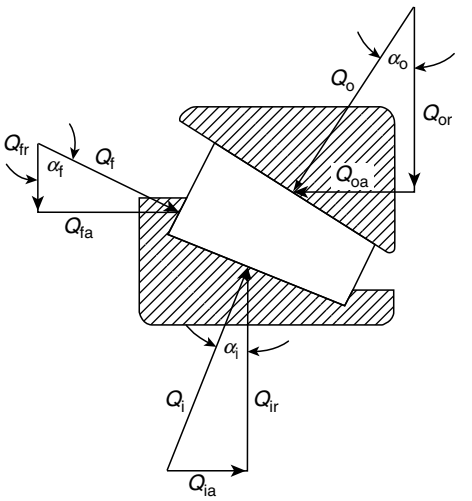

FIGURE 1.21 Roller loading in a tapered roller bearing.

In Equation 1.78 and Equation 1.79, coefficient $c_1 = -1$ and $c_2 = +1$. The equation for radial plane moment equilibrium of the roller is

$$w^2 \sum_{m=1}^{m=2} \sum_{\lambda=1}^{\lambda=k} q_{mj\lambda} \left[\lambda - \frac{1}{2}(k+1) \right] - R_{\mathrm{f}} Q_{\mathrm{f}j} = 0 \tag{1.80}$$

where R_{f} is the radius from the roller axis of rotation to the center of the roller end–flange contact. Equilibrium of actuating and resisting moments pertaining to roller skewing is given by

$$\frac{1}{2} l \mu Q_{\mathrm{f}j} - \frac{w^3 \xi_j}{(d_{\mathrm{m}} + D)} \sum_{m=1}^{m=2} \sum_{\lambda=1}^{\lambda=k} \left[\lambda - \frac{1}{2}(k+1) \right]^2 q_{mj\lambda} = 0 \tag{1.81}$$

The force and moment equilibrium equations with respect to the bearing inner ring are as follows:

$$F_{\mathrm{r}} - w \sum_{j=1}^{j=Z} \cos \psi_j \left[\sum_{\lambda=1}^{\lambda=k} q_{2j\lambda} \cos \alpha_2 - Q_{\mathrm{f}j} \cos \alpha_{\mathrm{f}} \right] = 0 \tag{1.82}$$

$$F_{\mathrm{a}} - w \sum_{j=1}^{j=Z} \left[\sum_{\lambda=1}^{\lambda=k} q_{2j\lambda} \sin \alpha_2 + Q_{\mathrm{f}j} \sin \alpha_{\mathrm{f}} \right] = 0 \tag{1.83}$$

$$M - w \sum_{j=1}^{j=Z} \cos \psi_j \left[\sum_{\lambda=1}^{\lambda=k} q_{2j\lambda} r_2 \cos \alpha_2 - Q_{\mathrm{f}j} (r_{\mathrm{f}z} \sin \alpha_{\mathrm{f}} - r_{\mathrm{f}x} \cos \alpha_{\mathrm{f}}) \right] = 0 \tag{1.84}$$

In these equations, the subscript 2 refers to the inner raceway.

1.5.3 Spherical Roller Bearings

Spherical roller bearings are internally self-aligning and therefore cannot carry moment loading. Moreover, for slow- or moderate-speed applications causing insignificant roller centrifugal forces, gyroscopic moments, and friction (see Chapter 2 and Chapter 3), rollers in spherical roller bearings will not exhibit a tendency to tilt. Therefore, the simpler analytical methods provided in Chapter 7 of the first volume of this book will yield accurate results. For spherical roller bearings that have asymmetrical contour rollers (for example, spherical roller thrust bearings) roller tilting and hence skewing are not eliminated. In this case for the purpose of analysis, the bearing may be considered a special type of tapered roller bearing with fully crowned rollers. Then, the methods of analysis discussed in Section 1.5.2 may be applied.

1.6 STRESSES IN ROLLER–RACEWAY NONIDEAL LINE CONTACTS

In practice, the contact between rollers and raceways is rarely an ideal line contact nor is it truly a series of independent laminae without interactions. The laminae approach used earlier is sufficient for determining the distribution of load within the contacts as the stresses due to truncation at the roller ends and other transitions with profile design cover very small areas. However, as bearing fatigue life is a function of the subsurface and hence surface contact stresses, the laminae approach is not always sufficient to estimate the contact stress distribution. Therefore, more sophisticated methods for the analysis of contact stresses are typically performed after the load distributions of the bearing have been estimated.

Starting with Thomas and Hoersch [8], several researchers have advanced the contact solution of Hertz for the nonideal situations. Using stress functions with Equation 6.7, Equation 6.9, Equation 6.10, Equation 6.13, and Equation 6.14 in the first volume of this book, Hartnett [9] defined the following relationship between the normal contact pressure at a location (x', y') and the surface deflection at a distant point (x, y) on an elastic half space as

$$w(x,y) = \left(\frac{1-\xi^2}{\pi E}\right) \frac{P(x',y')}{\sqrt{(x-x')^2+(y-y')^2}} \tag{1.85}$$

By breaking the contact surface into several small, rectangular patches of dimensions $2g$ along the y-axis and $2c$ along the x-axis directions with a node at the center of each patch, and assuming constant pressure over the area, Equation 1.85 can be integrated to determine the effect of contact pressure at a given node, i, on the deflection at another node, j. This is done by the use of influence coefficients, D_{ij}:

$$\begin{aligned}
D_{ij} = {} & \left(|x_i - x_j| + c\right) \ln \left[\frac{\left(|y_i - y_j| + g\right) + \sqrt{\left(|y_i - y_j| + g\right)^2 + \left(|x_i - x_j| + c\right)^2}}{\left(|y_i - y_j| - g\right) + \sqrt{\left(|y_i - y_j| - g\right)^2 + \left(|x_i - x_j| + c\right)^2}}\right] \\
& + \left(|y_i - y_j| + g\right) \ln \left[\frac{\left(|x_i - x_j| + c\right) + \sqrt{\left(|y_i - y_j| + g\right)^2 + \left(|x_i - x_j| + c\right)^2}}{\left(|x_i - x_j| - c\right) + \sqrt{\left(|y_i - y_j| + g\right)^2 + \left(|x_i - x_j| - c\right)^2}}\right] \\
& + \left(|x_i - x_j| - c\right) \ln \left[\frac{\left(|y_i - y_j| - g\right) + \sqrt{\left(|y_i - y_j| - g\right)^2 + \left(|x_i - x_j| - c\right)^2}}{\left(|y_i - y_j| + g\right) + \sqrt{\left(|y_i - y_j| + g\right)^2 + \left(|x_i - x_j| - c\right)^2}}\right] \\
& + \left(|y_i - y_j| - g\right) \ln \left[\frac{\left(|x_i - x_j| - c\right) + \sqrt{\left(|y_i - y_j| - g\right)^2 + \left(|x_i - x_j| - c\right)^2}}{\left(|x_i - x_j| + c\right) + \sqrt{\left(|y_i - y_j| - g\right)^2 + \left(|x_i - x_j| + c\right)^2}}\right]
\end{aligned} \tag{1.86}$$

Using the influence coefficients, the interference of two bodies in contact with a given approach δ is given by

$$\left\langle \delta - z_j - \frac{y^2}{2}\rho_y \right\rangle - \left(\frac{1-\xi_1^2}{\pi E_1} + \frac{1-\xi_2^2}{\pi E_2}\right) \sum_{i=1}^{i=n} D_{ij}\sigma_j = 0 \tag{1.87}$$

where z_j is the drop at location j from the highest point on the body due to profiling, and the term $\langle \delta - z_j - (y^2 / 2)\rho_y \rangle = 0$ when the computed value is less than zero. Finally, the equilibrium of applied contact force and the integral of the pressure over the contact yields

$$Q - 4gc \sum_{j=1}^{j=n} \sigma_j = 0 \tag{1.88}$$

Equation 1.86 and Equation 1.87 allow for the nonideal contact pressure to be estimated for any given contact geometry by varying δ until Equation 1.88 is satisfied within acceptable error limits.

1.7 FLEXIBLY SUPPORTED ROLLING BEARINGS

1.7.1 Ring Deflections

The preceding discussion of distribution of load among the bearing rolling elements pertains to bearings that have rigidly supported rings. Such bearings are assumed to be supported in infinitely stiff (rigid) housings and on solid shafts of rigid material. The deflections considered in the determination of load distribution were contact deformations. This assumption is an excellent approximation for most bearing applications.

In some radial bearing applications, however, the outer ring of the bearing may be supported at one or two azimuth positions only, and the shaft on which the inner ring is positioned may be hollow. The condition of two-point outer-ring support, as shown in Figure 1.22 and Figure 1.23, occurs in the planet gear bearings of a planetary gear power transmission system, and was analyzed by Jones and Harris [10]. In certain rolling mill applications, the backup roll bearings may be supported at only one point on the outer ring or possibly at two points as shown in Figure 1.24. These conditions were analyzed by Harris [11]. In certain high-speed radial bearings, to prevent skidding it is desirable to preload the rolling elements by using an elliptical raceway, thus achieving essentially two-point ring loading under conditions of light applied load. The case of a flexible outer ring and an elliptical inner ring was investigated by Harris and Broschard [12]. In each of these applications, the outer ring must be considered flexible to achieve a correct analysis of rolling element loading.

In many aircraft applications, to conserve weight the power transmission shafting is made hollow. In these cases, the inner-ring deflections will alter the load distribution from that considering only contact deformation.

To determine the load distribution among the rolling elements when one or both of the bearing rings is flexible, it is necessary to determine the deflections of a ring loaded at various

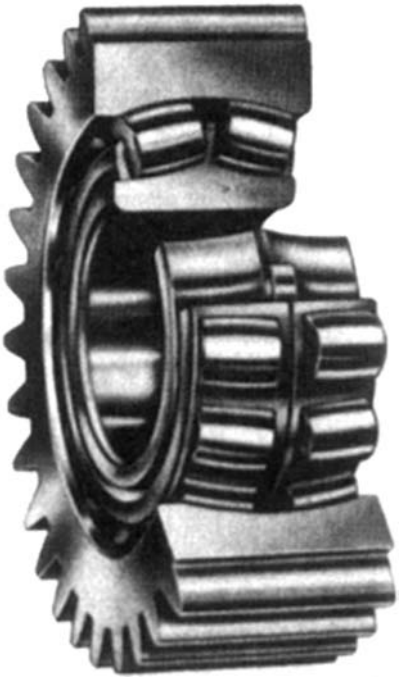

FIGURE 1.22 Planet gear bearing.

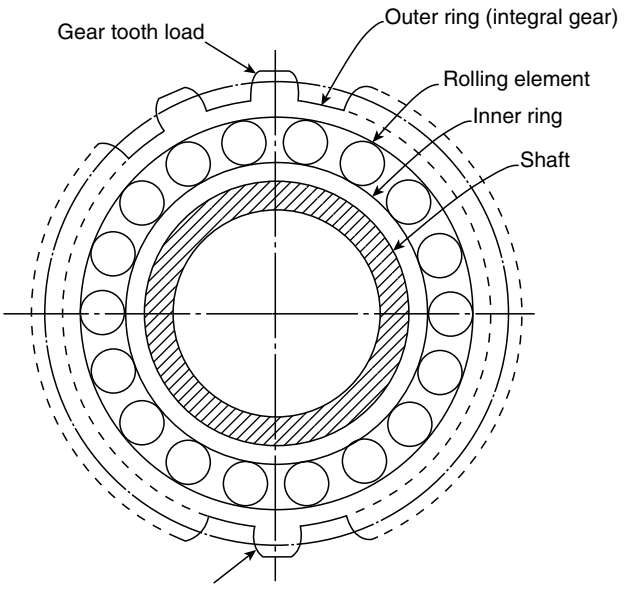

FIGURE 1.23 Planet gear bearing showing gear tooth loading.

points around its periphery. This analysis may be achieved by the application of classical energy methods for the bending of thin rings.

As an example of the method of analysis, consider a thin ring subjected to loads of equal magnitude equally spaced at angles $\Delta\psi$ (see Figure 1.25). According to Timoshenko [13], the

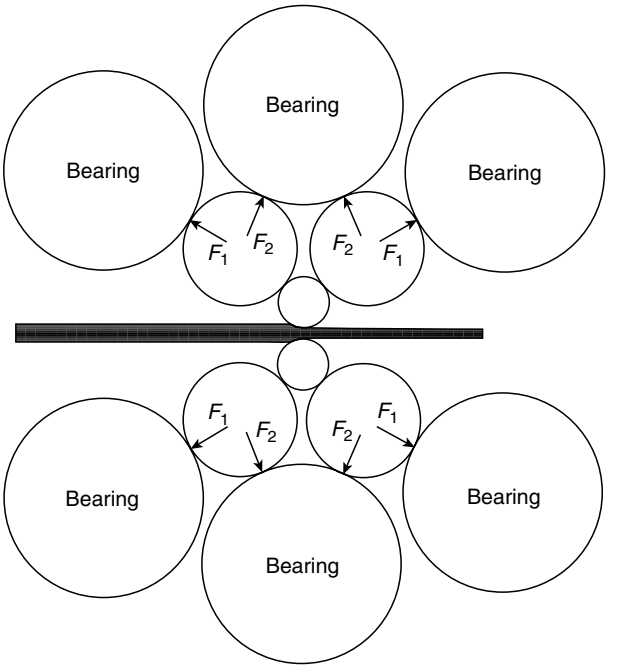

FIGURE 1.24 Cluster mill assembly showing backup roll bearing loading.

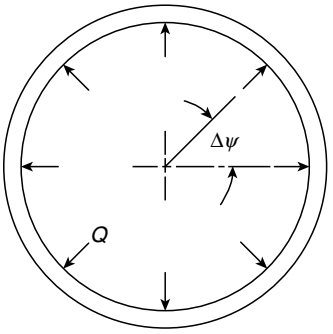

FIGURE 1.25 Thin ring loaded by equally spaced loads of equal magnitude.

differential equation describing radial deflection u for bending of a thin bar with a circular center line is

$$\frac{d^2u}{d\phi^2} + u = -\frac{M\Re^2}{EI} \tag{1.89}$$

where I is the section moment of inertia in bending and E is the modulus of elasticity. It can be shown that the complete solution of Equation 1.89 consists of a complementary solution and a particular solution. The complementary solution is

$$u_c = C_1 \sin\phi + C_2 \cos\phi \tag{1.90}$$

where C_1 and C_2 are arbitrary constants.

Consider that the ring is cut at two positions: at the position of loading, $\phi = \frac{1}{2}\Delta\psi$, and at the position $\phi = 0$, midway between the loads. The loads required to maintain equilibrium over the section are shown in Figure 1.26. From Figure 1.26 it can be seen that since horizontal forces are balanced,

$$Q = 2F_0 \sin\phi \tag{1.91}$$

or

$$F_0 = \frac{Q}{2\sin\phi} \tag{1.92}$$

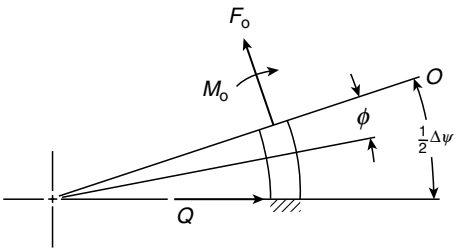

FIGURE 1.26 Loading of section of thin ring between $0 \leq \phi \leq \frac{1}{2}\Delta\psi$.

The moment at any angle ϕ between 0 and $\frac{1}{2}\Delta\psi$ is apparently

$$M = M_0 - F_0\Re(1 - \cos\phi) \tag{1.93}$$

or

$$M = M_0 - \frac{Q\Re}{2\sin\phi}(1 - \cos\phi) \tag{1.94}$$

Since the section at $\phi = 0$ is midway between loads, it cannot rotate. According to Castigliano's theorem [13] the angular rotation at any section is

$$\theta = \frac{\partial U}{\partial M} \tag{1.95}$$

where U is the strain energy in the beam at the position of loading. Timoshenko [13] shows that for a curved beam

$$U = \int_0^{\phi} \frac{M^2\Re}{2EI}\mathrm{d}\phi \tag{1.96}$$

At $\phi = 0$, $M = M_0$ and since the section is constrained from rotation,

$$\frac{\partial U}{\partial M_0} = 0 = \frac{\Re}{EI}\int_0^{1/2\Delta\psi} M\frac{\partial M}{\partial M_0}\mathrm{d}\phi \tag{1.97}$$

Substituting Equation 1.94 into Equation 1.97 and integrating yields

$$M_0 = \frac{Q\Re}{2}\left[\frac{1}{\sin\left(\frac{1}{2}\Delta\psi\right)} - \frac{2}{\Delta\psi}\right] \tag{1.98}$$

Hence,

$$M = \frac{Q\Re}{2}\left[\frac{\cos\phi}{\sin(\frac{1}{2}\Delta\psi)} - \frac{2}{\Delta\psi}\right] \tag{1.99}$$

Equation 1.99 may be substituted for M in Equation 1.89 such that the particular solution is

$$u_\mathrm{p} = \frac{Q\Re^3}{2EI}\left[\frac{\phi\sin\phi}{2\sin(\frac{1}{2}\Delta\psi)} - \frac{1}{\Delta\psi}\right] \tag{1.100}$$

The complete solution is

$$u = u_\mathrm{c} + u_\mathrm{p} = C_1\sin\phi + C_2\cos\phi - \frac{Q\Re^3}{2EI}\left[\frac{\phi\sin\phi}{2\sin(\frac{1}{2}\Delta\psi)} - \frac{1}{\Delta\psi}\right] \tag{1.101}$$

Because the sections at $\phi = 0$ and $\phi = \frac{1}{2}\Delta\psi$ do not rotate,

$$\left.\frac{du}{d\phi}\right|_{\phi=0} = 0; \quad C_1 = 0$$

$$\left.\frac{du}{d\phi}\right|_{\phi=\Delta\psi/2} = 0; \quad C_2 = -\frac{Q\Re^3}{4EI\sin(\frac{1}{2}\Delta\psi)}\left[\frac{1}{2}\Delta\psi\ \mathrm{ctn}\left(\frac{1}{2}\Delta\psi\right)+1\right]$$

Hence, the radial deflection at any angle ϕ between $\phi = 0$ and $\phi = \frac{1}{2}\Delta\psi$ is

$$u = \frac{Q\Re^3}{2EI}\left\{\frac{2}{\Delta\psi} - \left[\frac{\Delta\psi\cos(\frac{1}{2}\Delta\psi)}{4\sin^2(\frac{1}{2}\Delta\psi)} + \frac{1}{2\sin(\frac{1}{2}\Delta\psi)}\right]\cos\phi - \frac{\phi\sin\phi}{2\sin(\frac{1}{2}\Delta\psi)}\right\} \tag{1.102}$$

Equation 1.102 may be expressed in another format as follows:

$$u = C_\phi Q \tag{1.103}$$

where C_ϕ are influence coefficients dependent on angular position and ring dimensions.

$$C_\phi = \frac{\Re^3}{2EI}\left\{\frac{2}{\Delta\psi} - \left[\frac{\Delta\psi\cos(\frac{1}{2}\Delta\psi)}{4\sin^2(\frac{1}{2}\Delta\psi)} + \frac{1}{2\sin(\frac{1}{2}\Delta\psi)}\right] \times \cos\phi - \frac{\phi\sin\phi}{2\sin(\frac{1}{2}\Delta\psi)}\right\} \tag{1.104}$$

Lutz [14], using procedures similar to those described earlier, developed influence coefficients for various conditions of point loading of a thin ring. These coefficients have been expressed in infinite series format for the sake of simplicity of use.

For a thin ring loaded by forces of equal magnitude symmetrically located about a diameter as shown in Figure 1.27, the following equation yields radial deflections:

$${}_Q u_i = {}_Q C_{ij} Q \tag{1.105}$$

where

$${}_Q C_{ij} = \mp \frac{2\Re^3}{\pi EI}\sum_{m=2}^{m=\infty}\frac{\cos m\psi_j\ \cos m\psi_i}{(m^2-1)^2} \tag{1.106}$$

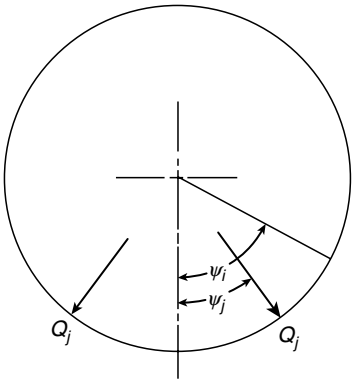

FIGURE 1.27 Thin ring loaded by forces of equal magnitude located asymmetrically about a diameter.

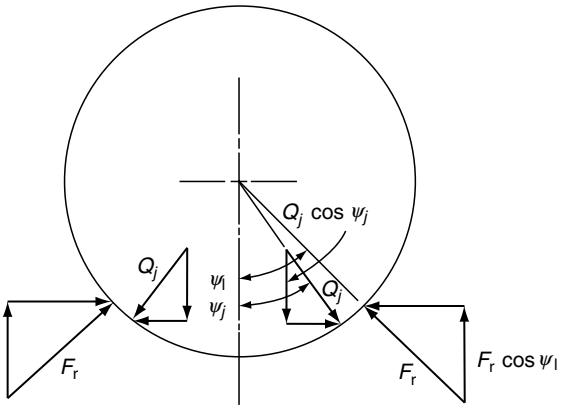

FIGURE 1.28 Thin ring showing equilibrium of forces.

The negative sign in Equation 1.106 is used for internal loads and the positive sign is used for external loads. Equation 1.105 defines radial deflection at angle ψ_i caused by Q_j at position angle ψ_j. When rolling element loads Q_j are such that a rigid body translation δ_1 of the ring occurs in the direction of an applied load, Equation 1.105 is not self-sufficient in establishing a solution; however, a directional equilibrium equation may be used in conjunction with Equation 1.105 to determine the translatory movement. Referring to Figure 1.28, the appropriate equilibrium equation is as follows:

$$F_r \cos \psi_1 - Q_j \cos \psi_j = 0 \tag{1.107}$$

In the planet gear bearing application demonstrated in Figure 1.23, the gear tooth loads may be resolved into tangential forces, radial forces, and moment loads at $\psi = 90°$ (see Figure 1.29). The ring radial deflections at angle ψ_i due to tangential forces F_t are given by

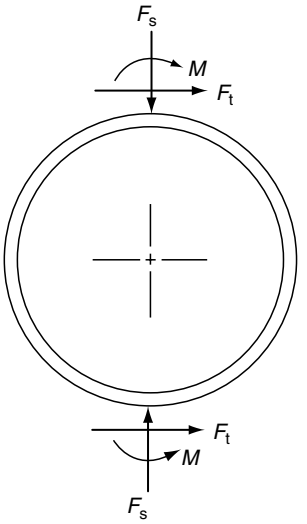

FIGURE 1.29 Resolution of gear tooth loading on outer ring.

$$ {}_{\mathrm{t}}u_i = {}_{\mathrm{t}}C_i F_{\mathrm{t}} \tag{1.108} $$

where

$$ {}_{\mathrm{t}}C_i = \frac{2\Re^3}{\pi EI} \sum_{m=2}^{m=\infty} \frac{\sin\frac{m\pi}{2}\cos m\psi_i}{m(m^2-1)^2} \tag{1.109} $$

Equation 1.108 is not self-sufficient and an appropriate equilibrium equation must be used to define a rigid ring translation.

The separating forces F_{s} are self-equilibrating and thus do not cause a rigid ring translation. The radial deflections at angles ψ_i are given by

$$ {}_{\mathrm{s}}u_i = {}_{\mathrm{s}}C_i F_{\mathrm{s}} \tag{1.110} $$

where

$$ {}_{\mathrm{s}}C_i = \frac{2\Re^3}{\pi EI} \sum_{m=2}^{m=\infty} \frac{\cos\frac{m\pi}{2}\cos m\psi_i}{(m^2-1)^2} \tag{1.111} $$

Note that Equation 1.111 is a special case of Equation 1.106 where position angle ψ_j is 90° and loads Q_j are external.

Similarly, the moment loads applied at $\psi = 90°$ are self-equilibrating. The radial deflections are given by

$$ {}_{\mathrm{M}}u_i = {}_{\mathrm{M}}C_i M \tag{1.112} $$

where

$$ {}_{\mathrm{M}}C_i = \frac{2\Re^2}{\pi EI} \sum_{m=2}^{m=\infty} \frac{\sin\frac{m\pi}{2}\cos m\psi_i}{m(m^2-1)^2} \tag{1.113} $$

To find the ring radial deflections at any regular position due to the combination of applied and resisting loads, the principle of superposition is used. Hence for the planet gear bearing, the radial deflection at any angular position ψ_i is the sum of the radial deflections due to each individual load, that is,

$$ u_i = {}_{\mathrm{s}}u_i + {}_{\mathrm{M}}u_i + {}_{\mathrm{t}}u_i + {}_{\mathrm{Q}j}u_i \tag{1.114} $$

or

$$ u_i = {}_{\mathrm{s}}C_i F_{\mathrm{s}} + {}_{\mathrm{M}}C_i M + {}_{\mathrm{t}}C_i F_{\mathrm{t}} + \sum {}_{Q}C_{ij} Q_j \tag{1.115} $$

1.7.2 Relative Radial Approach of Rolling Elements to the Ring

A load may not be transmitted through a rolling element unless the outer ring deflects sufficiently to consume the radial clearance at the angular position occupied by the rolling element. Furthermore, because a contact deformation is caused by loading of the rolling element, the ring

deflections cannot be determined without considering these contact deformations. Therefore, the loading of a rolling element at angular position ψ_j depends on the relative radial clearance. The relative radial approach of the rings includes the translatory movement of the center of the outer ring relative to the initial center of that ring, whose position is fixed in space. Hence, for the planet gear bearing, the relative radial approach at angular position ψ_j is

$$\delta_i = \delta_1 \cos \psi_i + u_i \tag{1.116}$$

From Equation 1.12, the relative radial approach is related to the rolling element load as follows:

$$Q_j = \begin{Bmatrix} K(\delta_j - r_j)^n & \delta_j > r_j \\ 0 & \delta_j \le r_j \end{Bmatrix} \tag{1.117}$$

where r_j is the radial clearance at angular position ψ_j. Here, r_j is the sum of $P_d/2$ and the condition of ring ellipticity.

1.7.3 Determination of Rolling Element Loads

Using the example of the planet gear bearing, the complete loading of the outer ring is shown in Figure 1.30, which also illustrates the rigid ring translation δ_1. Combining Equation 1.115 through Equation 1.117 yields

$$\delta_i - \delta_1 \cos\psi_i - {}_{\mathrm{s}}C_i F_{\mathrm{s}} - {}_{\mathrm{M}}C_i M - {}_{\mathrm{t}}C_i F_{\mathrm{t}} - iK \sum_{j=2}^{j=Z/2+2} {}_{Q}C_{ij}(\delta_j - r_j)^n = 0 \tag{1.118}$$

The required equilibrium equation is

$$F_{\mathrm{t}} - iK \sum_{j=2}^{j=Z/2+2} \tau_j (\delta_j - r_j)^n \cos \psi_j = 0 \tag{1.119}$$

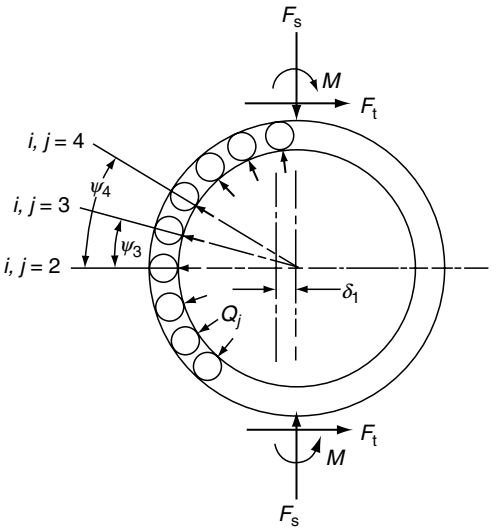

FIGURE 1.30 Total loading of outer ring in planet gear bearing.

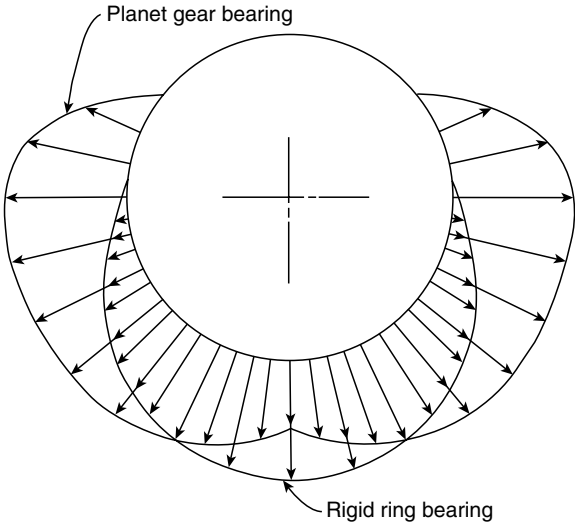

FIGURE 1.31 Comparison of load distribution for a rigid ring bearing and planet gear bearing.

considering the symmetry about the diameter parallel to the load. In Equation 1.119, $\tau_j = 0.5$ if the rolling element is located at $\psi_j = 0°$ or at $\psi_j = 180°$; otherwise $\tau_j = 1$.

Equation 1.118 and Equation 1.119 constitute a set of simultaneous nonlinear equations that may be solved by numerical analysis. The Newton–Raphson method is recommended.

Using these methods, the unknowns δ_j and hence Q_j can be determined at each rolling element location. Figure 1.31 shows a typical distribution of load among the rollers in a planet gear bearing compared with that of a rigid ring bearing subjected to a radial load of $2F_t$. For the backup roll bearings of Figure 1.24 supporting individual line loads F_1, Figure 1.32 compares the load distribution to that of a bearing that has rigid rings. Figure 1.33 shows

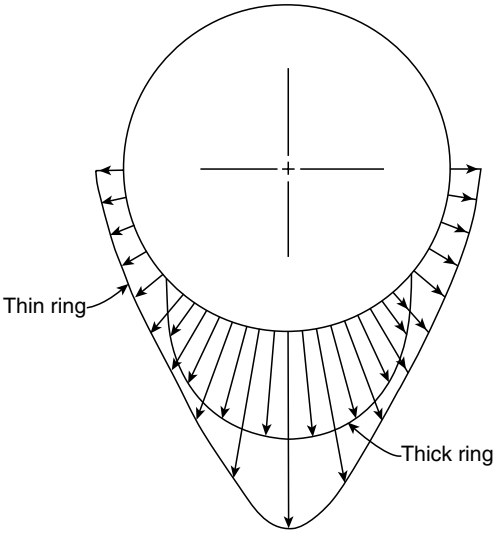

FIGURE 1.32 Comparison of load distribution of thin and thick outer rings, point-loaded backup roll bearing.

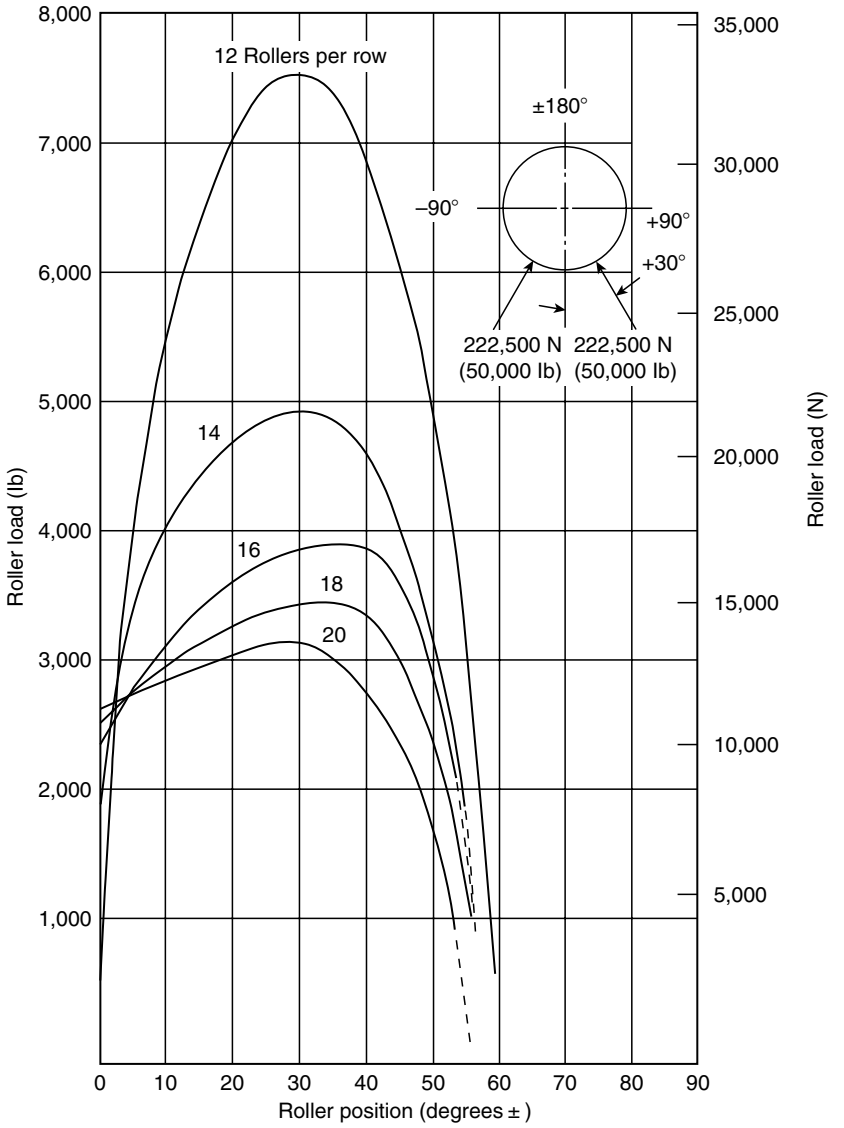

FIGURE 1.33 Roller load vs. number of rollers and position. 222,500 N (50,000 lb) at ±30°, inner dimensions constant. Outer-ring section thickness increases as the number of rollers is increased and roller diameter is subsequently decreased.

typical load distributions for the backup roll bearing of Figure 1.24, which supports paired line loads F_2. Figure 1.34 from Ref. [15], which is a photoelastic study of a similarly loaded bearing, verifies the data in Figure 1.33.

1.7.4 Finite Element Methods

To specify ring deflections, closed form integral analytical methods as well as influence coefficients calculated using infinite series techniques have been indicated for ring shapes, which are assumed simple both in circumference and cross-section in the previous discussions. For more complex structures, the finite element methods of calculations can be used to obtain

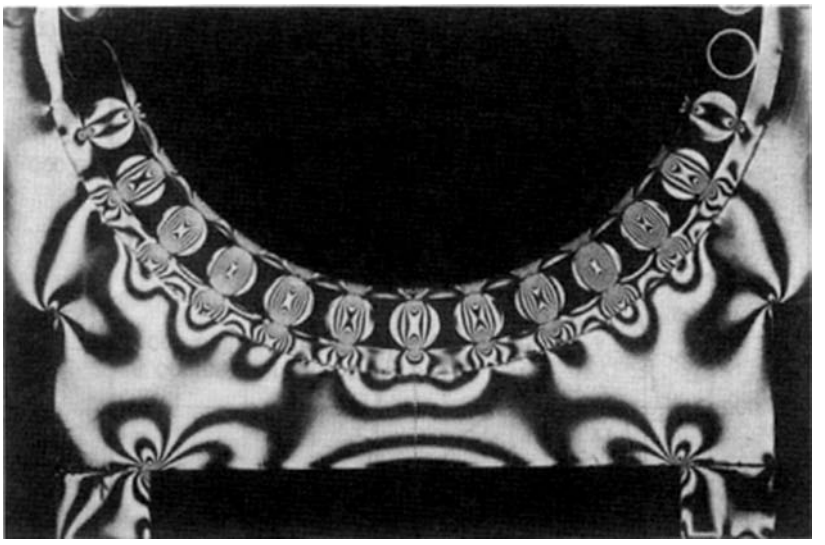

FIGURE 1.34 Photoelastic study of a roller bearing supporting loads aligned at approximately $\pm 30°$ to the bearing axis. (From Eimer, H., Aus dem Gebiet der Wälzlagertechnik, Semesterentwurf, Technische Hochschule, München, June 1964.)

a solution whose accuracy depends only on the fineness of the grid selected to represent the structure.

In finite element methods a function, customarily a polynomial, is chosen to define uniquely the displacement in each element (in terms of nodal displacements). The element

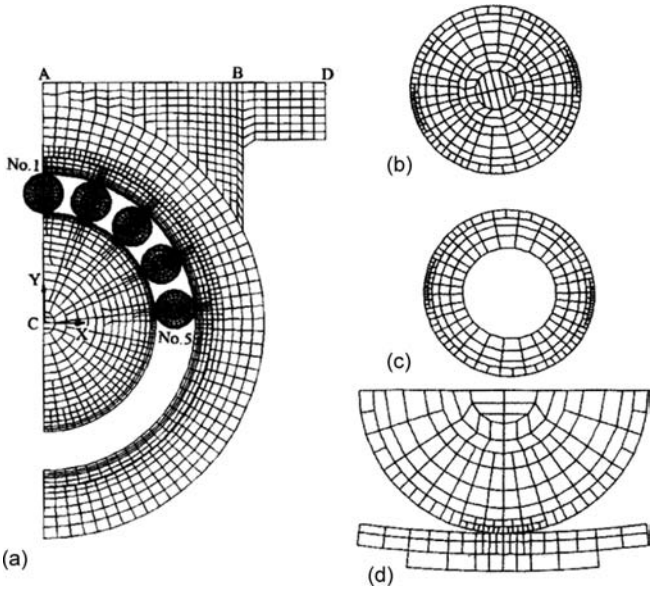

FIGURE 1.35 Finite element meshes for analyzing (a) cylindrical roller bearing rings, (b) solid rollers, (c) hollow rollers, and (d) contact zone. (From Zhao, H., *ASME Trans. J. Tribol.*, 120, 134–139, January 1998. With permission.)

stiffness matrix is obtained from equilibrium. The stiffness matrix of the complete structure is assembled, the boundary conditions are introduced, and solution of the resulting matrix equation produces the nodal displacements. A digital computer is required to solve the displacements and load distribution accurately in a rolling bearing mounted on a flexible support. Figure 1.35 from Zhao [16] shows the grids used to analyze a flexibly mounted cylindrical roller bearing assuming both solid and hollow rollers. The load distribution would be similar to that indicated in Figure 1.34.

Bourdon et al. [17,18] provided a method to define stiffness matrices for use in standard finite element models to analyze rolling element bearing loads and deflections, and the loading and deflections of the mechanisms in which they are used. For flexible mechanisms and bearing support systems, they demonstrated the importance of considering the overall mechanical system rather than only the local system in the vicinity of the bearings.

1.8 CLOSURE

The methods developed in this chapter enable the calculation of the internal load distribution of bearings in applications beyond those considered in bearing manufacturers' catalogs as supported by the load rating standards. It must be remembered, however, that these methods still pertain to bearing applications involving slow to moderate rotational speeds. At high speeds of rotation, ball and roller inertial loading (for example, centrifugal forces and gyroscopic moments) influence the internal load distribution, also affecting bearing deflections, friction forces, and moments. In this chapter, the discussion of the effect of speed on bearing performance has been limited to the determination of fatigue life in time units. Commencing with Chapter 3, the detailed effects of speed on overall bearing performance will be investigated.

REFERENCES

1. Jones, A., *Analysis of Stresses and Deflections*, New Departure Engineering Data, Bristol, CT, 1946.
2. Lundberg, G. and Sjövall, H., *Stress and Deformation in Elastic Contacts*, Pub. 4, Institute of Elasticity and Strength of Materials, Chalmers Inst. Tech., Gothenburg, Sweden, 1958.
3. Reussner, H., Druckflächenbelastnung und Overflächenverschiebung in Wälzkontact von Rotätionkörpern, Dissertation Schweinfurt, Germany, 1977.
4. Palmgren, A., *Ball and Roller Bearing Engineering*, 3rd ed., Burbank, Philadelphia, 1959.
5. Harris, T., The effect of misalignment on the fatigue life of cylindrical roller bearings having crowned rolling members, *ASME Trans. J. Lub. Technol.*, 294–300, April 1969.
6. Harris, T., The endurance of a thrust-loaded, double row, radial cylindrical bearing, *Wear*, 18, 429–438, 1971.
7. Harris, T., Kotzalas, M., and Yu, W.-K., On the causes and effects of roller skewing in cylindrical roller bearings, *Trib. Trans.*, 41(4), 572–578, 1998.
8. Thomas, H. and Hoersch, V., Stresses due to the pressure of one elastic solid upon another, *Univ. Illinois Bull.*, 212, July 15, 1930.
9. Hartnett, M., The analysis of contact stress in rolling element bearings, *ASME Trans. J. Lub. Technol.*, 101, 105–109, January 1979.
10. Jones, A. and Harris, T., Analysis of a rolling element idler gear bearing having a deformable outer race structure, *ASME Trans. J. Basic Eng.*, 273–278, June 1963.
11. Harris, T., Optimizing the design of cluster mill rolling bearings, *ASLE Trans.*, 7, April 1964.
12. Harris, T. and Broschard, J., Analysis of an improved planetary gear transmission bearing, *ASME Trans. J. Basic Eng.*, 457–462, September 1964.
13. Timoshenko, S., *Strength of Materials, Part I,* 3rd ed., Van Nostrand, New York, 1955.

14. Lutz, W., Discussion of Ref. 7, presented at ASME Spring Lubrication Symposium, Miami Beach, FL, June 5, 1962.
15. Eimer, H., *Aus dem Gebiet der Wälzlagertechnik*, Semesterentwurf, Technische Hochschule, München, June 1964.
16. Zhao, H., Analysis of load distributions within solid and hollow roller bearings, *ASME Trans. J. Tribol.*, 120, 134–139, January 1998.
17. Bourdon, A., Rigal, J., and Play, D., Static rolling bearing models in a C.A.D. environment for the study of complex mechanisms: Part I—rolling bearing model, *ASME Trans. J. Tribol.*, 121, 205–214, April 1999.
18. Bourdon, A., Rigal, J., and Play, D., Static rolling bearing models in a C.A.D. environment for the study of complex mechanisms: Part II—complete assembly model, *ASME Trans. J. Tribol.*, 121, 215–223, April 1999.

2 Bearing Component Motions and Speeds

LIST OF SYMBOLS

Symbol	Description	Units
a	Semimajor axis of projected contact ellipse	mm (in.)
b	Semiminor axis of projected contact ellipse	mm (in.)
d_m	Pitch diameter	mm (in.)
D	Ball or roller diameter	mm (in.)
f	r/D	
h	Center of sliding	mm (in.)
n	Rotational speed	rpm
n_m	Ball or roller orbital speed, cage speed	rpm
n_R	Ball or roller speed about its own axis	rpm
Q	Rolling element–raceway contact normal load	N (lb)
r	Raceway groove curvature radius	mm (in.)
r'	Rolling radius	mm (in.)
R	Radius of curvature of deformed surface	mm (in.)
v	Surface velocity	mm/sec (in./sec)
x	Distance in direction of major axis of contact	mm (in.)
y	Distance in direction of minor axis of contact	mm (in.)
α	Contact angle	°, rad
β	Ball pitch angle	°, rad
β'	Ball yaw angle	°, rad
γ	$D\cos\alpha/d_m$	
γ'	D/d_m	
θ_f	Flange angle	°, rad
ω	Rotational speed	rad/sec
ω_m	Orbital speed of ball or roller	rad/sec
ω_R	Speed of ball or roller about its own axis	rad/sec

Subscripts

f	Roller guide flange
i	Inner raceway
m	Orbital motion
o	Outer raceway

r	Radial direction
roll	Rolling motion
R	Rolling element
RE	Roller end
s	Spinning motion
sl	Sliding motion between flange and roller end
x	x Direction
z	z Direction

2.1 GENERAL

In Chapter 10 of the first volume of this handbook, equations were developed to calculate rolling element orbital speed and speed of the rolling element about its own axis. These equations were constructed using kinematical relationships based on simple rolling motion. Also, as discussed in Chapter 6 of the first volume of this handbook, when a load occurs between a rolling element and raceway, a contact surface is formed. When the rolling element rotates relative to the deformed surface, the simple rolling motion does not occur; rather, a combination of rolling and sliding motions occur. Hence, a system of complex equations needs to be developed to calculate the rolling element speeds.

Also, for angular-contact bearings, if the rolling motion does not occur on a line exactly parallel to the raceway, a parasitic motion called spinning occurs. Such a motion is pure sliding contributing significantly to bearing friction power loss. Finally, motions between roller ends and ring flanges in roller bearings are also pure sliding and can result in substantial power loss. In this chapter, these rolling/sliding relationships will be discussed together with the associated speeds.

2.2 ROLLING AND SLIDING

2.2.1 Geometrical Considerations

The only conditions that can sustain pure rolling between two contacting surfaces are:

1. Mathematical line contact under zero load
2. Line contact in which the contacting bodies are identical in length
3. Mathematical point contact under zero load

Even when these conditions are achieved, it is possible to have sliding. Sliding is then a condition of overall relative movement of the rolling body over the contact area.

The motion of a rolling element with respect to the raceway consists of a rotation about the generatrix of motion. If the contact surface is a straight line in one of the principal directions, the generatrix of motion may intersect the contact surface at one point only, as in Figure 2.1. The of angular velocity ω, which acts in the plane of the contact surface, produces rolling motion. As indicated in Figure 2.2, the component ω_s of angular velocity ω that acts normal to the surface

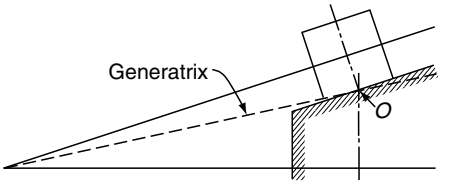

FIGURE 2.1 Roller–raceway contact; generatrix of motion pierces contact surface.

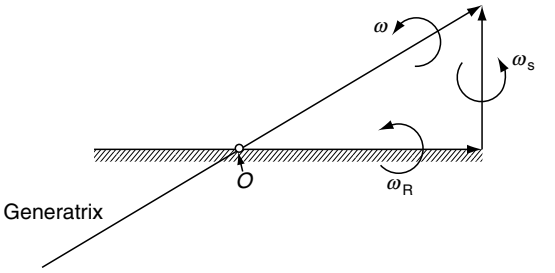

FIGURE 2.2 Resolution of angular velocities into rolling and spinning motions.

causes a spinning motion about a point of pure rolling O. The instantaneous direction of sliding in the contact zone is shown in Figure 2.3.

In ball bearings with nonzero contact angles between balls and raceways, during operation at any shaft or outer-ring speed, a gyroscopic moment occurs on each loaded ball, tending to cause a sliding motion. In most applications, because of relatively slow input speeds or heavy loading, such gyroscopic moments and hence motions can be neglected. In high-speed applications with oil-film lubrication between balls and raceways, such motions will occur.

The sliding velocity due to gyroscopic motion is given by (see Figure 2.4)

$$v_g = \tfrac{1}{2}\omega_g D \tag{2.1}$$

The sliding velocities caused by gyroscopic motion and spinning of the balls are vectorially additive such that at some distance h and O they cancel each other. Thus,

$$v_g = \omega_s h \tag{2.2}$$

and

$$h = \frac{D}{2} \times \frac{\omega_g}{\omega_s} \tag{2.3}$$

The distance h defines the center of sliding about which a rotation of angular velocity ω_s occurs. This center of sliding (spinning) may occur within or outside of the contact surface. Figure 2.5 shows the pattern of sliding lines in the contact area for simultaneous rolling, spinning, and gyroscopic motion in a ball bearing operating under a heavy load and at moderate speed. Figure 2.6, which corresponds to low-load and high-speed conditions (however, not considering skidding*), indicates that the center of sliding is outside of the

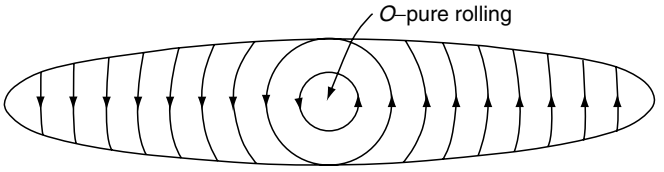

FIGURE 2.3 Contact ellipse showing sliding lines and point of pure rolling.

*Skidding is a very gross sliding condition occurring generally in oil-film lubricated ball and roller bearings operating under relatively light load at very high speed or rapid accelerations and decelerations. When skidding occurs, cage speed will be less than predicted by Equation 8.9 for bearings with inner ring rotation.

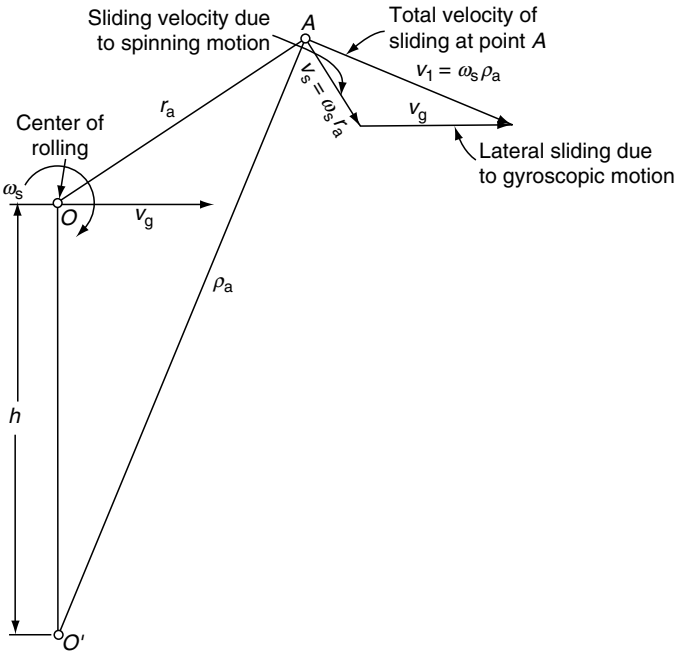

FIGURE 2.4 Velocities of sliding at arbitrary point A in contact area.

contact surface and sliding occurs over the entire contact surface. The distance h between the centers of contact and sliding is a function of the magnitude of the gyroscopic moment that can be compensated by contact surface friction forces.

2.2.2 Sliding and Deformation

Even when the generatrix of motion apparently lies in the plane of the contact surface, as for radial cylindrical roller bearings, sliding on the contact surface can occur when a roller is under load. In accordance with the Hertzian radius of the contact surface in the direction transverse to motion, the contact surface has a harmonic mean profile radius, which means that the contact surface is not plane, but generally curved as shown in Figure 2.7 for a radial bearing.* The generatrix of motion, parallel to the tangent plane of the center of the contact

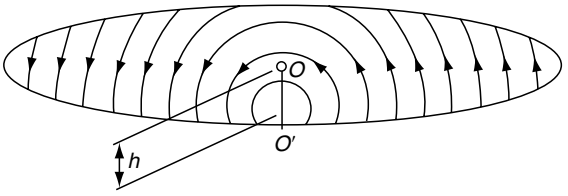

FIGURE 2.5 Sliding lines in contact area for simultaneous rolling, spinning, and gyroscopic motions—low-speed operation of a ball bearing.

*The illustration pertains to a spherical roller under relatively light load, that is, the contact ellipse major axis does not exceed the roller length.

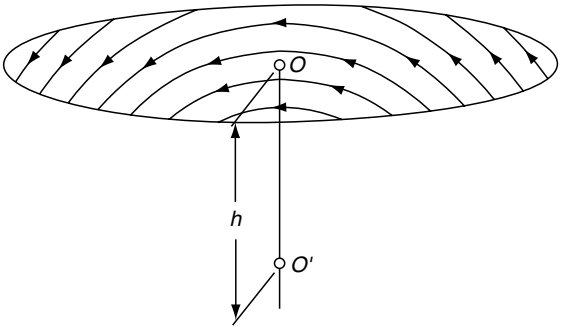

FIGURE 2.6 Sliding lines in contact area for simultaneous rolling, spinning, and gyroscopic motions—high-speed operation of a ball bearing (not considering skidding).

surface, therefore, pierces the contact surface at two points at which rolling occurs. Because the rigid rolling element rotates with a singular angular velocity about its axis, surface points at different radii from the axis have different surface velocities; only two of them that are symmetrically disposed about the roller geometrical center can exhibit pure rolling motion. In Figure 2.7 points within area *A–A* slide backward with regard to the direction of rolling and points outside of *A–A* slide forward with respect to the direction of rolling. Figure 2.8 shows the pattern of sliding lines in the elliptical contact area.

If the generatrix of motion is angled with respect to the tangent plane at the center of the contact surface, the center of rolling is positioned asymmetrically in the contact ellipse and, depending on the angle of the generatrix to the contact surface, one point or two points of intersection may occur at which rolling obtains. Figure 2.9 shows the sliding lines for this condition.

For a ball bearing in which rolling, spinning, and gyroscopic motions occur simultaneously, the pattern of sliding lines in the elliptical contact area is as shown in Figure 2.10 and Figure 2.11. More detailed information on sliding in the elliptical contact area may be found in the work by Lundberg [1].

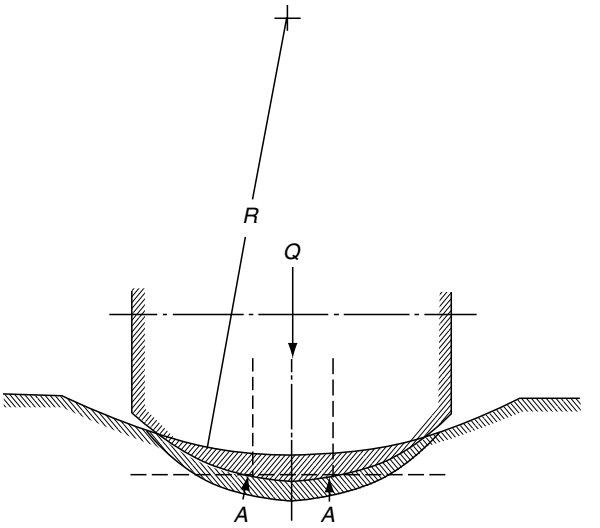

FIGURE 2.7 Roller–raceway contact showing harmonic mean radius and points of rolling *A–A*.

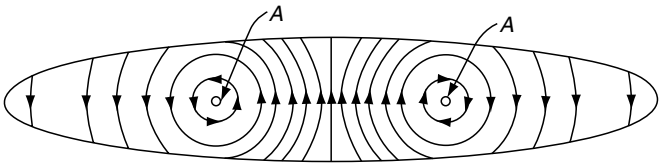

FIGURE 2.8 Sliding lines in contact area of Figure 2.7.

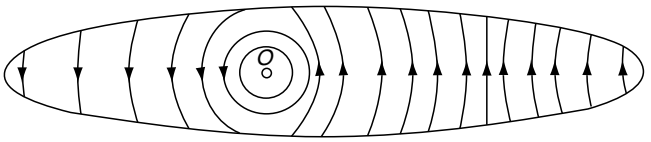

FIGURE 2.9 Sliding lines for rolling element–raceway contact area when load is applied; generatrix of motion pierces contact area.

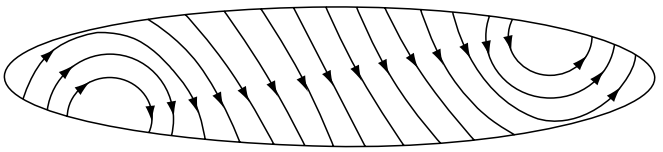

FIGURE 2.10 Sliding lines for ball–raceway contact area for simultaneous rolling, spinning, and gyroscopic motions—high-load and low-speed operation of an angular-contact ball bearing.

2.3 ORBITAL, PIVOTAL, AND SPINNING MOTIONS IN BALL BEARINGS

2.3.1 General Motions

Figure 2.12 illustrates the speed vector for a single ball in a bearing. The bearing is associated with the coordinate system x, y, z with the bearing axis collinear with the x axis. In Figure 2.12, the ball center O' is displaced angular distance ψ from the xz plane, and the x' axis passing through O' is distance $\frac{1}{2}\,d_{\mathrm{m}}$ from, and parallel to, the x axis. The bearing is seen to rotate at speed ω about the x axis while the ball rotates at speed ω_{R} about an axis displaced at pitch and yaw angles β and β', respectively, from the x' axis. Hence, the ball orbits the bearing axis at speed ω_{m}. If the balls are completely constrained by a cage, then ω_{m} is the cage speed.

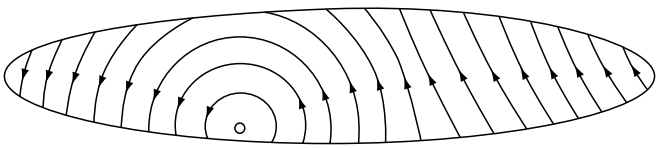

FIGURE 2.11 Sliding lines for ball–raceway contact area for simultaneous rolling, spinning, and gyroscopic motions—low-load and high-speed operation of an angular-contact ball bearing (not considering skidding).

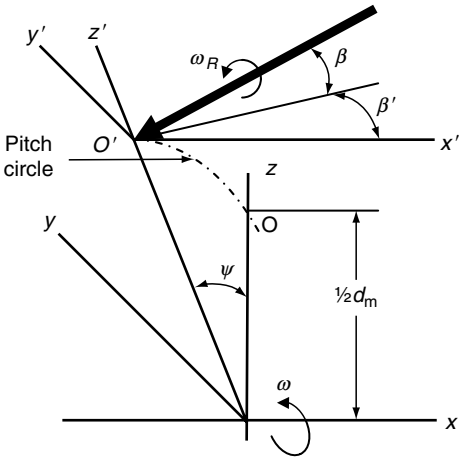

FIGURE 2.12 Ball speed vector in a nonzero ball–raceway contact.

In the same bearing, Figure 2.13 shows a ball contacting the outer raceway such that the normal force Q between the ball and the raceway is distributed over an elliptical surface defined by the projected major and minor axes $2a_o$ and $2b_o$, respectively. The radius of curvature of the deformed pressure surface as defined by Hertz is

$$R_o = \frac{2r_o D}{2r_o + D} \tag{2.4}$$

where r_o is the outer raceway groove curvature radius. In terms of curvature f_o,

$$R_o = \frac{2f_o D}{2f_o + 1} \tag{2.5}$$

Assume for the present purpose that the ball center is fixed in space and that the outer raceway rotates with angular speed ω_o. (The vector of ω_o is perpendicular to the plane of rotation and therefore collinear with the x axis.) Moreover, it can be seen from Figure 2.12 that ball rotational speed ω_R has components $\omega_{x'}$ and $\omega_{z'}$ lying in the plane of the paper when $\psi = 0$.

Because of the deformation at the pressure surface defined by a_o and b_o, the radius from the ball center to the raceway contact point varies in length as the contact ellipse is traversed from $+a_o$ to $-a_o$. Therefore, because of symmetry about the minor axis of the contact ellipse, pure rolling motion of the ball over the raceway occurs at most at two points. The radius at which pure rolling occurs is defined as r'_o and must be determined by methods of contact deformation analysis.

It can be seen from Figure 2.13 that the outer raceway has a component $\omega_o \cos \alpha_o$ of the angular velocity vector in a direction parallel to the major axis of the contact ellipse. Therefore, a point (x_o, y_o) on the outer raceway has a linear velocity v_{1o} in the direction of rolling as defined below:

$$v_{1o} = -\frac{d_m \omega_o}{2} - \left\{ (R_o^2 - x_o^2)^{1/2} - (R_o^2 - a_o^2)^{1/2} + \left[\left(\frac{D}{2} \right)^2 - a_o^2 \right]^{1/2} \right\} \omega_o \cos \alpha_o \tag{2.6}$$

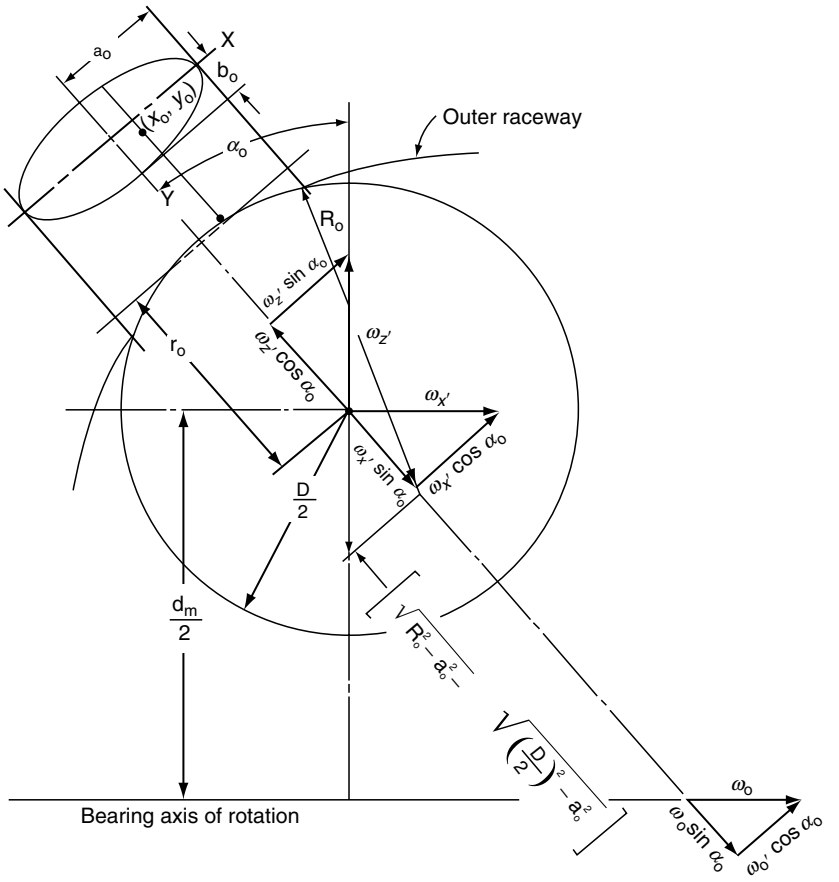

FIGURE 2.13 Outer raceway contact.

Similarly, the ball has angular velocity components, $\omega_{x'} \cos \alpha_o$ and $\omega_{z'} \sin \alpha_o$, of the angular velocity vector ω_R lying in the plane of the paper and parallel to the major axis of the contact ellipse. Thus, a point (x_o, y_o) on the ball has a linear velocity v_{2o} in the direction of rolling defined as follows:

$$v_{2o} = -(\omega_{x'} \cos \alpha_o + \omega_{z'} \sin \alpha_o) \times \left\{ (R_o^2 - x_o^2)^{1/2} - (R_o^2 - a_o^2)^{1/2} + \left[\left(\frac{D}{2} \right)^2 - a_o^2 \right]^{1/2} \right\} \quad (2.7)$$

Slip or sliding of the outer raceway over the ball in the direction of rolling is determined by the difference between the linear velocities of raceway and ball. Hence,

$$v_{yo} = v_{1o} - v_{2o} \quad (2.8)$$

or

$$v_{yo} = o - \frac{d_m \omega_o}{2} + (\omega_{x'} \cos \alpha_o + \omega_{z'} \sin \alpha_o - \omega_o \cos \alpha_o) \times \left\{ (R_o^2 - x_o^2)^{1/2} - (R_o^2 - a_o^2)^{1/2} + \left[\left(\frac{D}{2} \right)^2 - a_o^2 \right]^{1/2} \right\} \quad (2.9)$$

Additionally, the ball angular velocity vector ω_R has a component $\omega_{y'}$ in a direction perpendicular to the plane of the paper. This component causes a slip v_{xo} in the direction transverse to the rolling, that is, in the direction of the major axis of the contact ellipse. This slip velocity is given by

$$v_{xo} = -\omega_{y'}\left\{(R_o^2 - x_o^2)^{1/2} - (R_o^2 - a_o^2)^{1/2} + \left[\left(\frac{D}{2}\right)^2 - a_o^2\right]^{1/2}\right\} \tag{2.10}$$

From Figure 2.13, it can be observed that both the ball angular velocity vectors $\omega_{x'}$ and $\omega_{z'}$, and the raceway angular velocity vector ω_o have components normal to the contact area. Hence, there is a rotation about a normal to the contact area; in other words, a spinning of the outer raceway relative to the ball, the net magnitude of which is given by

$$\omega_{so} = -\omega_o \sin\alpha_o + \omega_{x'} \sin\alpha_o - \omega_{z'} \cos\alpha_o \tag{2.11}$$

From Figure 2.12, it can be determined that

$$\omega_{x'} = \omega_R \cos\beta \cos\beta' \tag{2.12}$$

$$\omega_{y'} = \omega_R \cos\beta \sin\beta' \tag{2.13}$$

$$\omega_{z'} = \omega_R \sin\beta \tag{2.14}$$

Substitution of Equation 2.12 and Equation 2.14 into Equation 2.9 through Equation 2.11 yields

$$\begin{aligned} v_{yo} = &-\frac{d_m \omega_o}{2} + \left\{(R_o^2 - x_o^2)^{1/2} - (R_o^2 - a_o^2)^{1/2} + \left[\left(\frac{D}{2}\right)^2 - a_o^2\right]^{1/2}\right\} \\ &\times \left(\frac{\omega_R}{\omega_o}\cos\beta\cos\beta'\cos\alpha_o + \frac{\omega_R}{\omega_o}\sin\beta\sin\alpha_o - \cos\alpha_o\right)\omega_o \end{aligned} \tag{2.15}$$

$$v_{xo} = -\left\{(R_o^2 - x_o^2)^{1/2} - (R_o^2 - a_o^2)^{1/2} + \left[\left(\frac{D}{2}\right)^2 - a_o^2\right]^{1/2}\right\}\omega_o\left(\frac{\omega_R}{\omega_o}\right)\cos\beta\sin\beta' \tag{2.16}$$

$$\omega_{so} = \left(\frac{\omega_R}{\omega_o}\cos\beta\cos\beta'\sin\alpha_o - \frac{\omega_R}{\omega_o}\sin\beta\cos\alpha_o - \sin\alpha_o\right)\omega_o \tag{2.17}$$

Note that at the radius of rolling r'_o on the ball, the translation velocity of the ball is identical to that of the outer raceway. From Figure 2.13, therefore,

$$\left(\frac{d_m}{2\cos\alpha_o} + r'_o\right)\omega_o \cos\alpha_o = r'_o(\omega_{x'}\cos\alpha_o + \omega_{z'}\sin\alpha_o) \tag{2.18}$$

Substituting Equation 2.12 and Equation 2.13 into Equation 2.18, and rearranging the terms yields

$$\frac{\omega_R}{\omega_o} = \frac{(d_m/2) + r'_o\cos\alpha_o}{r'_o(\cos\beta\cos\beta'\cos\alpha_o + \sin\beta\sin\alpha_o)} \tag{2.19}$$

A similar analysis may be applied to the inner raceway contact as illustrated in Figure 2.14. The following equations can be determined:

$$v_{yi} = -\frac{d_m \omega_i}{2} - \left\{ (R_i^2 - x_i^2)^{1/2} - (R_i^2 - a_i^2)^{1/2} + \left[\left(\frac{D}{2} \right)^2 - a_i^2 \right]^{1/2} \right\} \times \left(\frac{\omega_R}{\omega_i} \cos\beta \cos\beta' \cos\alpha_i + \frac{\omega_R}{\omega_i} \sin\beta \sin\alpha_i - \cos\alpha_i \right) \omega_i \tag{2.20}$$

$$v_{xi} = -\left\{ (R_i^2 - x_i^2)^{1/2} - (R_i^2 - a_i^2)^{1/2} + \left[\left(\frac{D}{2} \right)^2 - a_i^2 \right]^{1/2} \right\} \omega_i \left(\frac{\omega_R}{\omega_i} \right) \cos\beta \sin\beta' \tag{2.21}$$

$$\omega_{si} = \left(-\frac{\omega_R}{\omega_i} \cos\beta \cos\beta' \sin\alpha_i + \frac{\omega_R}{\omega_i} \sin\beta \cos\alpha_i + \sin\alpha_i \right) \omega_i \tag{2.22}$$

$$\frac{\omega_R}{\omega_i} = \frac{-(d_m/2) + r_i' \cos\alpha_i}{r_i' (\cos\beta \cos\beta' \cos\alpha_i + \sin\beta \sin\alpha_i)} \tag{2.23}$$

If instead of the ball center fixed in space, the outer raceway is fixed, then the ball center must orbit about the center 0 of the fixed coordinate system with an angular speed $\omega_m = -\omega_o$.

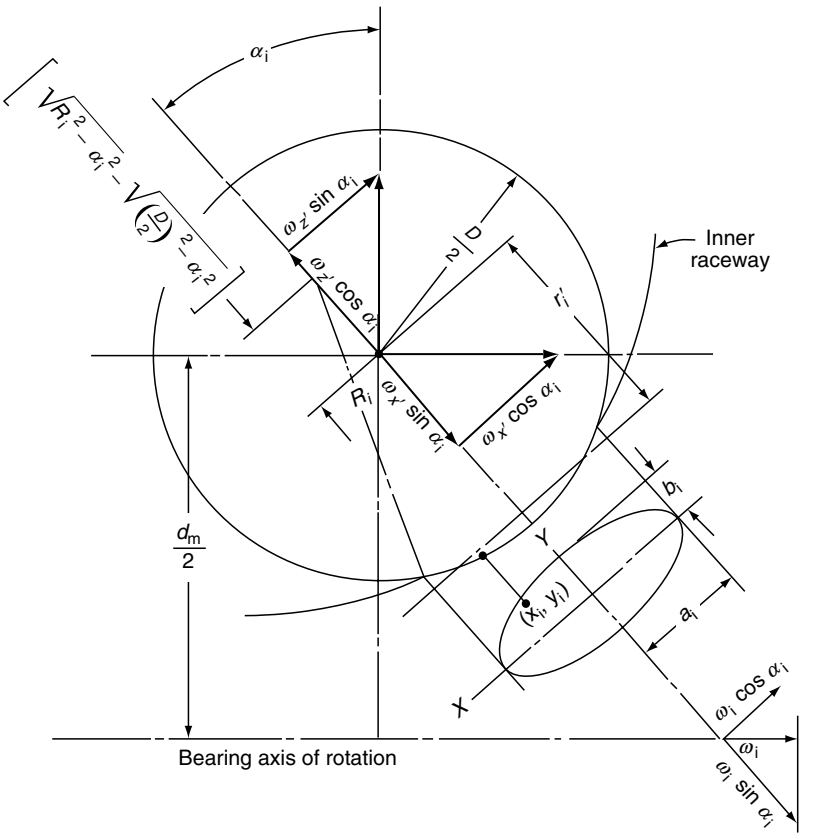

FIGURE 2.14 Inner raceway contact.

Therefore, the inner raceway must rotate with absolute angular speed $\omega = \omega_i + \omega_m$. By using these relationships, the relative angular speeds ω_i and ω_o can be described in terms of the absolute angular speed of the inner raceway as follows:

$$\omega_i = \frac{\omega}{1 + \dfrac{r'_o[(d_m/2) - r'_i \cos\alpha_i](\cos\beta\cos\beta'\cos\alpha_o + \sin\beta\sin\alpha_o)}{r'_i[(d_m/2) + r'_o \cos\alpha_o](\cos\beta\cos\beta'\cos\alpha_i + \sin\beta\sin\alpha_i)}} \tag{2.24}$$

$$\omega_o = \frac{-\omega}{1 + \dfrac{r'_i[(d_m/2) + r'_o \cos\alpha_o](\cos\beta\cos\beta'\cos\alpha_i + \sin\beta\sin\alpha_i)}{r'_o[(d_m/2) - r'_i \cos\alpha_i](\cos\beta\cos\beta'\cos\alpha_o + \sin\beta\sin\alpha_o)}} \tag{2.25}$$

Further,

$$\omega_R = \frac{-\omega}{\dfrac{r'_o(\cos\beta\cos\beta'\cos\alpha_o + \sin\beta\sin\alpha_o)}{(d_m/2) + r'_o\cos\alpha_o} + \dfrac{r'_i(\cos\beta\cos\beta'\cos\alpha_i + \sin\beta\sin\alpha_i)}{(d_m/2) - r'_i\cos\alpha_i}} \tag{2.26}$$

Similarly, if the outer raceway rotates with absolute angular speed ω and the inner raceway is stationary, $\omega_m = \omega_i$ and $\omega = \omega_m + \omega_o$. Therefore,

$$\omega_o = \frac{\omega}{1 + \dfrac{r'_i[(d_m/2) + r'_o \cos\alpha_o](\cos\beta\cos\beta'\cos\alpha_i + \sin\beta\sin\alpha_i)}{r'_o[(d_m/2) - r'_i \cos\alpha_i](\cos\beta\cos\beta'\cos\alpha_o + \sin\beta\sin\alpha_o)}} \tag{2.27}$$

$$\omega_i = \frac{-\omega}{1 + \dfrac{r'_o[(d_m/2) - r'_i \cos\alpha_i](\cos\beta\cos\beta'\cos\alpha_o + \sin\beta\sin\alpha_o)}{r'_i[(d_m/2) + r'_o \cos\alpha_o](\cos\beta\cos\beta'\cos\alpha_i + \sin\beta\sin\alpha_i)}} \tag{2.28}$$

$$\omega_R = \frac{\omega}{\dfrac{r'_o(\cos\beta\cos\beta'\cos\alpha_o + \sin\beta\sin\alpha_o)}{(d_m/2) + r'_o\cos\alpha_o} + \dfrac{r'_i(\cos\beta\cos\beta'\cos\alpha_i + \sin\beta\sin\alpha_i)}{(d_m/2) - r'_i\cos\alpha_i}} \tag{2.29}$$

Inspection of the final equations relating to the relative motions of the balls and raceways reveals the following unknown quantities: r'_o, r'_i, β, β', α_i, and α_o. It is apparent that an analysis of the forces and moments acting on each ball will be required to evaluate the unknown quantities. As a practical matter, however, it is sometimes possible to avoid this lengthy procedure requiring digital computation by using the simplifying assumption that a ball will roll on one raceway without spinning and spin and roll simultaneously on the other raceway. The raceway on which only rolling occurs is called the "controlling" raceway. Moreover, it is also possible to assume that gyroscopic pivotal motion is negligible; some criteria for this will be discussed.

2.3.2 No Gyroscopic Pivotal Motion

In the event that gyroscopic rotation is minimal, the angle β' approaches 0° (see Figure 2.12). Therefore, the angular rotation $\omega_{y'}$ is zero and further

$$\omega_{x'} = \omega_R \cos\beta \tag{2.30}$$

$$\omega_{z'} = \omega_R \sin\beta \tag{2.31}$$

A second consequence of $\beta' = 0$ is that

$$\frac{\omega_R}{\omega_o} = \frac{(d_m/12) + r'_o \cos\alpha_o}{r'_o(\cos\alpha_o \cos\beta + \sin\beta \sin\alpha_o)} \tag{2.32}$$

and

$$\frac{\omega_R}{\omega_i} = \frac{-(d_m/2) + r'_i \cos\alpha_i}{r'_i(\cos\beta \cos\alpha_i + \sin\beta \sin\alpha_i)} \tag{2.33}$$

2.3.3 Spin-to-Roll Ratio

Assuming for this calculation that r_i, r_o, and $\frac{1}{2} D$ are essentially equal, the ball rolling speed relative to the outer raceway is

$$\omega_{roll} = -\omega_o \frac{d_m}{D} = -\frac{\omega_o}{\gamma'} \tag{2.34}$$

From Equation 2.17 for negligible gyroscopic moment ($\beta' = 0$),

$$\omega_{so} = \omega_R \cos\beta \sin\alpha_o - \omega_R \sin\beta \cos\alpha_o - \omega_o \sin\alpha_o \tag{2.35}$$

or

$$\omega_{so} = \omega_R \sin(\alpha_o - \beta) - \omega_o \sin\alpha_o \tag{2.36}$$

Dividing by ω_{roll} according to Equation 2.34 yields

$$\left(\frac{\omega_s}{\omega_{roll}}\right)_o = -\gamma' \frac{\omega_R}{\omega_o} \sin(\alpha_o - \beta) + \gamma' \sin\alpha_o \tag{2.37}$$

According to Equation 2.32, replacing $2r'_o/d_m$ by γ':

$$\frac{\omega_R}{\omega_o} = \frac{1 + \gamma' \cos\alpha_o}{\gamma'(\cos\beta \cos\alpha_o + \sin\beta \sin\alpha_o)} \tag{2.38}$$

or

$$\frac{\omega_R}{\omega_o} = \frac{1 + \gamma' \cos\alpha_o}{\gamma' \cos(\alpha_o - \beta)} \tag{2.39}$$

Therefore, substitution of Equation 2.39 into Equation 2.37 yields

$$\left(\frac{\omega_s}{\omega_{roll}}\right)_o = -(1 + \gamma' \cos\alpha_o) \tan(\alpha_o - \beta) + \gamma' \sin\alpha_o \tag{2.40}$$

Similarly, for an inner raceway contact,

$$\left(\frac{\omega_s}{\omega_{roll}}\right)_i = (1 - \gamma' \cos\alpha_i)\tan(\alpha_i - \beta) + \gamma' \sin\alpha_i \tag{2.41}$$

2.3.4 Calculation of Rolling and Spinning Speeds

Even assuming that gyroscopic speed ω_y' is zero, the use of Equation 2.40 and Equation 2.41 depends on the knowledge of the ball–raceway contact angles α_i and α_o, and ball speed vector pitch angle β. In Chapter 3, means to calculate β_i and β_o in high-speed, angular-contact ball bearings will be demonstrated. Those equations assume that ball orbital speed ω_m and ball speed about its own axis, ω_R, are known. Unfortunately, unless the ball speed vector pitch angle β is known, the solution of the set of simultaneous equations involving contact deformations, contact angles, and ball speeds cannot be achieved. To determine these parameters in the most elegant manner, ball–raceway friction forces as functions of ball and raceway speeds need to be introduced. This situation will also be investigated later in this text.

In the absence of using a complete set of normal and friction forces and moment balances to solve for speeds, Jones [2] made the simplifying assumption that a ball contacting both inner and outer raceways rolls and spins on one of these raceways and simply rolls on the opposing raceway. He based this assumption on his interpretation of experimental data obtained from gas turbine engine main-shaft ball bearings. The raceway on which pure rolling was assumed to occur was called the controlling raceway; the phenomenon was called raceway control. Assuming the condition that outer raceway control occurs, spinning speed $\omega_{so} = 0$, and substitution of Equation 2.32 into Equation 2.17 yields

$$\tan\beta = \frac{\frac{1}{2}d_m \sin\alpha_o}{\frac{1}{2}d_m \cos\alpha_o + r_o'} \tag{2.42}$$

As $r_o' \approx \frac{1}{2}D$ and $D/d_m = \gamma'$, Equation 2.42 becomes

$$\tan\beta = \frac{\sin\alpha_o}{\cos\alpha_{o+\gamma'}} \tag{2.43}$$

Having defined ball speed vector pitch angle β, it is possible to solve the remaining speed equations.

For high-speed operations of very lightly loaded, oil-lubricated, angular-contact ball bearings, Figure 2.15 taken from Ref. [3] indicates that ball–outer raceway spinning speed ω_{so} tends toward zero, approximating the outer raceway control condition. As the applied thrust load increases to normal operating magnitudes, ω_{so} though less than ω_{si} is substantial. This allows one to infer that outer raceway control is a condition that occurs only in a very limited manner for oil-lubricated ball bearings.

Harris [4] also investigated the performance of thrust-loaded, solid-film lubricated, angular-contact ball bearings of the same dimensions assuming a constant coefficient of friction. Figure 2.16 from that analysis demonstrates that outer raceway control does not tend to occur in that application either.

Notwithstanding the above observations, it is of interest to carry the Jones analysis [2] to completion since it has been used for several decades with apparently little negative impact on bearing design.

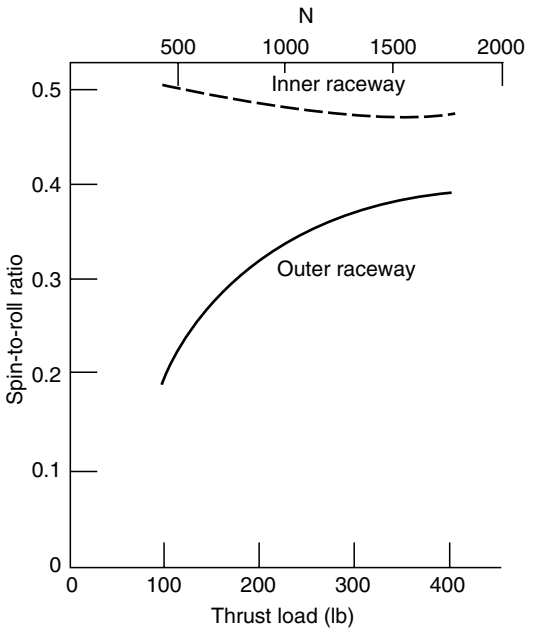

FIGURE 2.15 Spin-to-roll ratio vs. thrust load for an oil-lubricated, angular-contact ball bearing.

From Equation 2.24 and Equation 2.25, setting β' equal to 0 and substituting for Equation 2.43, the ratio between ball and raceway angular velocities is determined:

$$\frac{\omega_R}{\omega} = \frac{\pm 1}{\left(\dfrac{\cos\alpha_o + \tan\beta\sin\alpha_o}{1+\gamma'\cos\alpha_o} + \dfrac{\cos\alpha_i + \tan\beta\sin\alpha_i}{1-\gamma'\cos\alpha_i}\right)\gamma'\cos\beta} \tag{2.44}$$

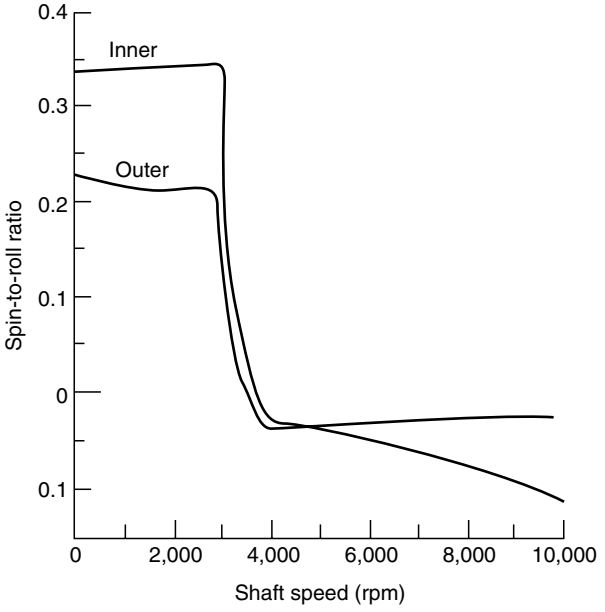

FIGURE 2.16 Spin-to-roll ratio vs. shaft speed for a thrust-loaded, angular-contact ball bearing operating with a solid-film lubricant having a constant coefficient of friction.

The upper sign pertains to outer raceway rotation and the lower sign to inner raceway rotation.

Again, using the condition of outer raceway control as established in Equation 2.43, it is possible to determine the ratio of ball orbital angular velocity to raceway speed. For a rotating inner raceway $\omega_m = -\omega_o$; therefore, from Equation 2.25 for β' equal to 0,

$$\frac{\omega_m}{\omega} = \frac{1}{1 + \dfrac{(1 + \gamma' \cos\alpha_o)(\cos\alpha_i + \tan\beta \sin\alpha_i)}{(1 - \gamma' \cos\alpha_i)(\cos\alpha_o + \tan\beta \sin\alpha_o)}} \tag{2.45}$$

Equation 2.45 is based on the valid assumption that $r_0 \approx r_i \approx D/2$. Similarly, for a rotating outer raceway and by Equation 2.28,

$$\frac{\omega_m}{\omega} = \frac{1}{1 + \dfrac{(1 - \gamma' \cos\alpha_i)(\cos\alpha_o + \tan\beta \sin\alpha_o)}{(1 + \gamma' \cos\alpha_o)(\cos\alpha_i + \tan\beta \sin\alpha_i)}} \tag{2.46}$$

Substitution of Equation 2.43 describing the condition of outer raceway control into Equation 2.45 and Equation 2.46 establishes the equations of the required ratio ω_m/ω. Hence, for a bearing with rotating inner raceway,

$$\frac{\omega_m}{\omega} = \frac{1 - \gamma' \cos\alpha_i}{1 + \cos(\alpha_i - \alpha_o)} \tag{2.47}$$

For a bearing with a rotating outer raceway,

$$\frac{\omega_m}{\omega} = \frac{\cos(\alpha_i - \alpha_o) + \gamma' \cos\alpha_i}{1 + \cos(\alpha_i + \alpha_o)} \tag{2.48}$$

As indicated above, Equation 2.43, Equation 2.44, Equation 2.47, and Equation 2.48 are valid only when ball gyroscopic pivotal motion is negligible, that is, $\beta' = 0$.

2.3.5 Gyroscopic Motion

Palmgren [5] inferred that in an oil-lubricated, angular-contact ball bearing, gyroscopic motions of the balls can be prevented. He stated that the coefficient of sliding friction may be as low as 0.02 and that gyroscopic motion will not occur if the following relationship is satisfied:

$$M_g > 0.02QD \tag{2.49}$$

where Q is the ball–raceway normal load. Jones [2] mentioned that a coefficient of friction from 0.06 to 0.07 suffices for most ball bearing applications to prevent sliding. Both of these statements are inaccurate.

It has been shown that a ball in an angular-contact ball bearing is capable of experiencing both orbital speed ω_m about the bearing axis and speed ω_R about its own axis that is canted at pitch angle β to the x' axis. The latter axis is parallel to the bearing axis (see Figure 2.12). It has been further demonstrated that sliding motion in the direction of rolling motion occurs in the ball–raceway contacts. Additionally, owing to the nonzero contact angle, spinning motion occurs. Given the presence of these sliding motions, it is most probable that motion initiated

by a gyroscopic moment will not be prevented. In other words, additional sliding in an orthogonal direction (gyroscopic motion) will occur simultaneously. Subsequent analysis employing complete force and moment balances for each ball shows the speed of ball gyroscopic motion $\omega_{y'}$ to be very small compared with principal ball speed component $\omega_{x'}$ and relatively small compared to $\omega_{z'}$.

2.4 ROLLER END–FLANGE SLIDING IN ROLLER BEARINGS

2.4.1 Roller End–Flange Contact

Roller bearings react with axial roller loads through concentrated contacts between roller ends and flange. Tapered roller bearings and spherical roller bearings (with asymmetrical rollers) require such contact to react with the component of the raceway–roller contact load that acts in the roller axial direction. Some cylindrical roller bearing designs require roller end–flange contacts to react with skewing-induced or externally applied roller axial loads. As these contacts experience sliding motions between roller ends and flange, their contribution to overall bearing frictional heat generation becomes substantial. Furthermore, there are bearing failure modes associated with roller end–flange contact such as wear and smearing of the contacting surfaces. These failure modes are related to the ability of the roller end–flange contact to support the roller axial load under the prevailing speed and lubrication conditions within the contact. Both the frictional characteristics and load-carrying capability of roller end–flange contacts are highly dependent on the geometry of the contacting members.

2.4.2 Roller End–Flange Geometry

Numerous roller end and flange geometries have been used successfully in roller bearing designs. Typically, performance requirements as well as manufacturing considerations dictate the geometry incorporated into a bearing design. Most designs use either a flat (with corner radii) or sphere end roller contacting an angled flange. The angled flange surface can be described as a portion of a cone at an angle θ_f with respect to a radial plane perpendicular to the ring axis. This angle, known as the flange angle or flange layback angle, can be zero, indicating that the flange surface lies in the radial plane. Examples of cylindrical roller bearing roller end–flange geometries are shown in Figure 2.17. The flat end roller in Figure 2.17a under zero skewing conditions contacts the flange at a single point (in the vicinity of the intersection between the roller end flat and roller corner radius). As the roller skews, the point of contact travels along this intersection on the roller toward the tip of the flange, as shown in Figure 2.18b. If properly designed, a sphere end roller will contact the flange on the roller end sphere surface. For no skewing, the contact will be centrally positioned on the roller, as shown

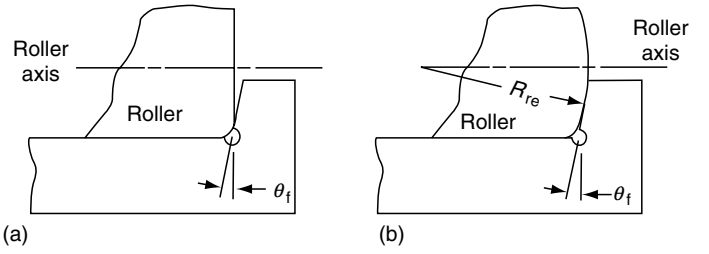

FIGURE 2.17 Cylindrical roller bearing, roller end–flange contact geometry. (a) Flat end roller. (b) Sphere end roller.

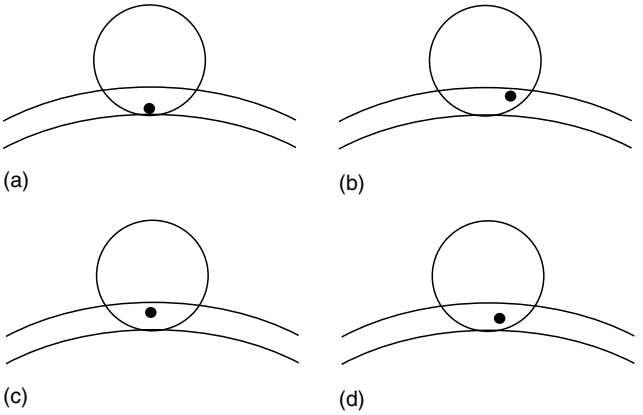

FIGURE 2.18 Cylindrical roller bearing, roller end–flange contact location for flat and sphere end rollers. (a) Flat end roller, zero skew angle. (b) Flat end roller, nonzero skew angle. (c) Sphere end roller, zero skew angle. (d) Sphere end roller, nonzero skew angle.

in Figure 2.18c. As the skewing angle is increased, the contact point moves off center and toward the flange tip, as shown in Figure 2.18d for a flanged inner ring. For typical designs, the sphere end roller contact location is less sensitive to skewing than a flat end roller contact.

The location of the roller end–flange contact has been determined analytically [6] for sphere end rollers contacting an angled flange. Consider the cylindrical roller bearing arrangement shown in Figure 2.19. The flanged ring coordinate system X_I, Y_I, Z_I and roller coordinate system X_i, Y_i, Z_i are indicated. The flange contact surface is modeled as a portion of a cone with an apex at point C as shown in Figure 2.20. The equation of this cone, expressed as a function of the x and y ring coordinates is

$$z = [(x - C)^2 \operatorname{ctn}^2 \theta_f - y^2]^{1/2} = f(x, y) \tag{2.50}$$

For a point of flange surface P_x, P_y, P_z, the equation of the surface normal at P can be expressed as

$$\left.\frac{x - P_x}{\dfrac{\partial f}{\partial x}}\right|_{x = P_x, y = P_y} = \left.\frac{y - P_y}{\dfrac{\partial f}{\partial y}}\right|_{x = P_x, y = P_y} = -(z - P_z) \tag{2.51}$$

The location of the origin of the roller end sphere radius is defined as point T with coordinates (T_x, T_y, T_z) expressed in the flanged ring coordinate system. As the resultant roller end–flange elastic contact force is normal to the end sphere surface, its line of action must pass through the sphere origin (T_x, T_y, T_z). Evaluating Equation 2.50 and Equation 2.51 at T yields the following three equations:

$$T_x - P_x = \frac{(T_z - P_z)(P_x - C)\operatorname{ctn}^2 \theta_f}{[(P_x - C)^2 \operatorname{ctn}^2 \theta_f - P_y^2]^{1/2}} \tag{2.52}$$

$$T_y - P_y = \frac{(T_z - P_z)P_y}{[(P_x - C)^2 \operatorname{ctn}^2 \theta_f - P_y^2]^{1/2}} \tag{2.53}$$

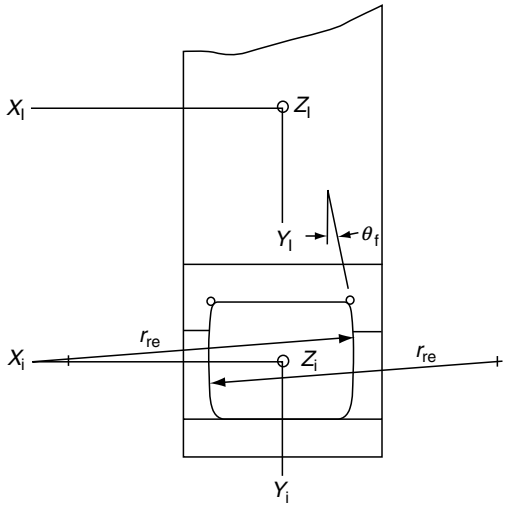

FIGURE 2.19 Cross-section through a cylindrical roller bearing that has a flanged inner ring.

$$P_z = [(P_x - C)^2 \operatorname{ctn}^2 \theta_f - P_y^2]^{1/2} \tag{2.54}$$

Equation 2.52 through Equation 2.54 contain three unknowns (P_x, P_y, P_z) and are sufficient to determine the theoretical point of contact between the roller end and flange. By introducing a fourth equation and unknown, however, namely the length of the line from points (T_x, T_y, T_z) to (P_x, P_y, P_z), the added benefit of a closed-form solution is obtained. The length of a line normal to the flange surface at the point (P_x, P_y, P_z), which joins this point with the sphere origin (T_x, T_y, T_z), is given by

$$\mathfrak{D} = [(T_x - P_x)^2 + (T_y - P_y)^2 + (T_z - P_z)^2]^{1/2} \tag{2.55}$$

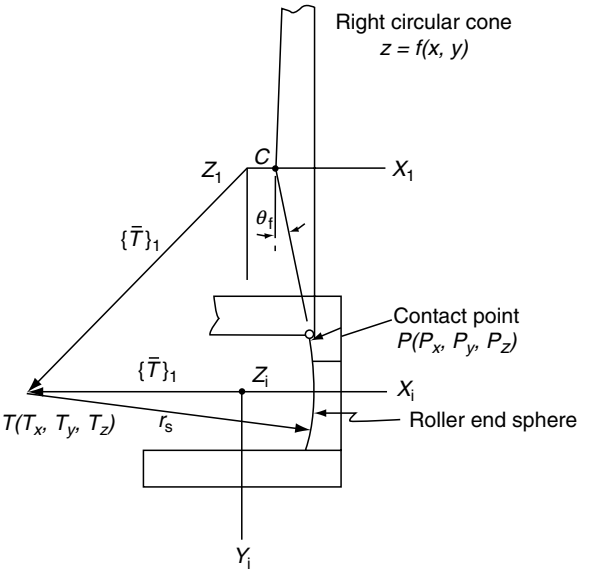

FIGURE 2.20 Coordinate system for calculation of roller end–flange contact location.

After algebraic reduction, $\mathfrak{D}$ is obtained from the positive root of the quadratic equation:

$$\mathfrak{D} = \frac{-\mathfrak{S} \pm (\mathfrak{S}^2 - 4\mathfrak{R}\mathfrak{T})^{1/2}}{2\mathfrak{R}} \tag{2.56}$$

where values for $\mathfrak{S}$, $\mathfrak{R}$, and $\mathfrak{T}$ are

$$\mathfrak{R} = \tan^2 \theta_f - 1$$

$$\mathfrak{S} = \frac{2\sin^2 \theta_f}{\cos \theta_f}[(T_x - C) - \tan \theta_f (T_y^2 + T_z^2)^{1/2}]$$

$$\mathfrak{T} = [(T_x - C) - \tan \theta_f (T_y^2 + T_z^2)^{1/2}]$$

The coordinates $P(P_x, P_y, P_z)$ are given by the following closed-form function of $\mathfrak{D}$:

$$P_x = T_y \tan \theta_f \left[1 + \left(\frac{T_z}{T_y}\right)^2\right]^{1/2} \left[1 - \frac{\mathfrak{D}}{(T_y^2 + T_z^2)^{1/2}}\right] + c \tag{2.57}$$

$$P_y = T_y \left[1 - \frac{\mathfrak{D} \sin \theta_f}{(T_y^2 + T_z^2)^{1/2}}\right] \tag{2.58}$$

$$P_z = T_z \left[1 - \frac{\mathfrak{D} \sin \theta_f}{(T_y^2 + T_z^2)^{1/2}}\right] \tag{2.59}$$

At a point of contact between the roller end and flange, $\mathfrak{D}$ is equal to the roller end sphere radius. Therefore, knowing the roller and flanged ring geometry as well as the coordinate location (with respect to the flanged ring coordinate system) of the roller end sphere origin, it is possible to calculate directly the theoretical roller end–flange contact location.

The analysis, although shown for a cylindrical roller bearing, is general enough to apply to any roller bearing that has sphere end rollers that contact a conical flange. Tapered and spherical roller bearings of this type may be treated if the sphere radius origin is properly defined.

These equations have several notable applications since flange contact location is of interest in bearing design and performance evaluation. It is desirable to maintain contact on the flange below the flange rim (including edge break) and above the undercut at the base of the flange. To do otherwise causes loading on the flange rim (or edge of undercut) and produces higher contact stresses and less than optimum lubrication of the contact. The preceding equations may be used to determine the maximum theoretical skewing angle for a cylindrical roller bearing if the roller axial play (between flanges) is known. Also, by calculating the location of the theoretical contact point, sliding velocities between roller ends and flange can be calculated and used in an estimate of roller end–flange contact friction and heat generation.

2.4.3 Sliding Velocity

The kinematics of a roller end–flange contact causes sliding to occur between the contacting members. The magnitude of the sliding velocity between these surfaces substantially affects friction, heat generation, and load-carrying characteristics of a roller bearing design. The sliding velocity is represented by the difference between the two vectors defining the linear velocities of the flange and the roller end at the point of contact. A graphical representation of